

Valence band states and polarized optical emission from nonpolar and semipolar III–nitride quantum well optoelectronic devices

Yuji Zhao¹, Robert M. Farrell¹, Yuh-Renn Wu², and James S. Speck^{1*}

¹Materials Department, University of California, Santa Barbara, CA 93106, U.S.A.

²Institute of Photonics and Optoelectronics and Department of Electrical Engineering, National Taiwan University, Taipei 10617, Taiwan
E-mail: speck@mrl.ucsb.edu

Received June 6, 2014; revised July 9, 2014; accepted July 15, 2014; published online September 25, 2014

Nonpolar and semipolar III–nitride quantum wells (QWs) and devices have been extensively studied due to their unique valence band (VB) structure and polarized optical emission. Unlike conventional *c*-plane oriented III–nitride QWs, the low crystal symmetry and unbalanced biaxial stress in nonpolar and semipolar QWs separates the topmost VBs and gives rise to polarized optical emission. Since the first experimental reports on nonpolar devices, research on this topic has progressed very rapidly and has covered nonpolar *m*-plane and *a*-plane QWs and devices as well as semipolar (11 $\bar{2}2$), (20 $\bar{2}1$), and (20 $\bar{2}\bar{1}$) QWs and devices. Issues such as strain, plane inclination angle (with respect to the *c*-plane), indium composition, temperature, and their impact on QW VB structure and device performance have been extensively studied. In this paper we review the physical background and theoretical analysis of the VB states and polarized optical emission of nonpolar and semipolar structures and discuss their potential impacts on optoelectronic devices. Experimental results for nonpolar and semipolar light-emitting diodes and laser diodes will be covered along with additional discussions on the potential applications and challenges related to their unique physical properties.

© 2014 The Japan Society of Applied Physics

1. Introduction

III–nitride semiconductors, including alloys of AlN, GaN, and InN, are remarkable materials with direct bandgaps that span the entire visible spectrum, which make them especially attractive for various optoelectronic applications.¹⁾ For example, InGaN based quantum well (QW) structures have enabled high performance light-emitting diodes (LEDs) and laser diodes (LDs) covering the violet ($\lambda \sim 400$ nm), blue ($\lambda \sim 450$ nm), and green ($\lambda \sim 525$ nm) spectral regions.^{1,2)} Commercially available InGaN LEDs and LDs are commonly grown on the polar *c*-plane of the wurtzite crystal due to the highly developed growth on (0001) sapphire, (0001) SiC and (111) Si. However, the performance of *c*-plane GaN optoelectronic devices is adversely affected by the presence of internal polarization-related electric fields.^{3–5)} Alternatively, growth of III–nitride structures on nonpolar and semipolar orientations has been proposed to eliminate these polarization-related issues on conventional *c*-plane devices.³⁾ In recent years, very high performance nonpolar and semipolar LEDs and LDs have been demonstrated.^{6–9)}

In addition to improved device performance, another unique and interesting feature of nonpolar and semipolar GaN LEDs is the polarized optical emission.¹⁰⁾ The three valence bands (VBs) of GaN are characterized with *x*-, *y*-, and *z*-directions corresponding to the nonpolar *a*-direction (11 $\bar{2}0$), the nonpolar *m*-direction ($\bar{1}\bar{1}00$), and the polar *c*-direction (0001), respectively. The top three VBs are derived from the nitrogen p_x , p_y , and p_z orbitals. The top two VBs, i.e., heavy hole and light hole, have the symmetry of $|X + iY\rangle$ and $|X - iY\rangle$, and the split-off band has the symmetry of $|Z\rangle$.^{11–15)} For *c*-plane structures such as InGaN/GaN or AlGaIn/GaN, the biaxial compressive stress in the coherently stressed alloy layer (InGaIn or AlGaIn) is isotropic in the *x*- and *y*-directions, producing an equal mixture of $|X\rangle$ and $|Y\rangle$ states in the heavy- and light-hole bands, which results in an isotropic light emission in the direction normal to the layer surface. For nonpolar structures, the unbalanced biaxial stress breaks the symmetry in the *x*–*y* plane, which splits the $|X \pm iY\rangle$ states into $|X\rangle$ and $|Y\rangle$ states. Therefore, the VBs of

nonpolar structure are reconstructed in the order of $|X\rangle$, $|Z\rangle$, and $|Y\rangle$ states with decreasing energy, which give rise to the polarized emission for emission from the free surface that is parallel to natural heterostructures such as QWs.^{11–15)} The polarization ratio (ρ) is used to quantify the degree of this polarization. For nonpolar *m*-plane structures, it is defined as $\rho = (I_a - I_c)/(I_a + I_c)$, where I_a and I_c are the integrated intensity values parallel to the *a*- and *c*-directions, respectively.¹⁵⁾ Since the first experimental report on nonpolar heterostructures, the research on this topic has progressed very rapidly and has covered nonpolar *m*-plane and *a*-plane QWs and devices as well as semipolar (11 $\bar{2}2$), (20 $\bar{2}1$), and (20 $\bar{2}\bar{1}$) QWs and devices.^{11–28)} Issues such as strain, plane inclination angle (with respect to *c*-plane), indium composition, temperature, and their impacts on QW VB states and device performance have been extensively studied. Key experimental reports on the topics are summarized in Table I,^{12–28)} while several theoretical calculations on electronic properties and band structures for III–nitride semiconductors are listed in Table II.^{29–38)} More detailed discussions are included in the following sections.

In this paper, we review recent research efforts on the VB states and the polarized optical emission for nonpolar and semipolar QW optoelectronic devices, and discuss their impact and potential opportunities for current device performance as well as future applications. Section 2 reviews the basic physics and theoretical background for the VB structures of nonpolar and semipolar InGaIn QWs, where the effects of strain, electrical polarization, and effective mass must be carefully discussed. Section 3 discusses the experimental measurements of the optical polarization and associated VB states and separations for nonpolar and semipolar LEDs. Topics such as device structure, measurement methods, recent experimental reports, and potential applications will be discussed. Section 4 discusses the impact of VB states and optical polarization on nonpolar and semipolar LD performance, including optical gain, birefringence, and waveguide orientation. Finally in Sect. 5 we summarize the paper and discuss the potential opportunities and future work on these topics.

Table I. List of experimental reports on VB separation and polarized emission on various nonpolar and semipolar QWs and devices. (QWs are mainly InGaN-based unless otherwise noted.)

Planes	Substrates	Structures	Methods	Years	Institutes
(1 $\bar{1}$ 00)	(1 $\bar{1}$ 00) SiC	3 μ m GaN	PL	1997	Domen et al., Fujitsu ¹²⁾
(1 $\bar{1}$ 00)	<i>r</i> -LiAlO ₂	1.22 μ m GaN	absorption, reflectance, and photoreflectance	2002	Ghosh et al., Paul-Drude-Institut ¹³⁾
(1 $\bar{1}$ 00)	<i>r</i> -LiAlO ₂	1.9 nm 20 QWs, QW structure	PL	2003	Sun et al., Paul-Drude-Institut ¹⁴⁾
(10 $\bar{1}$ 0)	(10 $\bar{1}$ 0) 4H-SiC	6 nm 5 QWs, LED structure	EL	2005	Gardner et al., Lumileds ¹⁵⁾
(10 $\bar{1}$ $\bar{3}$)	<i>m</i> -Sapphire	4 nm 5 QWs, LED structure	EL	2005	Sharma et al., UCSB ¹⁶⁾
(10 $\bar{1}$ 0)	(10 $\bar{1}$ 0) bulk GaN	4 nm 5 QWs, LED structure	EL	2005	Masui et al., UCSB ¹⁷⁾
(11 $\bar{2}$ 2)	(11 $\bar{2}$ 2) bulk GaN	3 nm SQW, LED structure	EL	2006	Funato et al., Kyoto Univ. and Nichia ¹⁸⁾
(10 $\bar{1}$ 0)	(10 $\bar{1}$ 0) bulk GaN	3 nm 3 QWs, LED structure	EL, back side of LEDs were polished	2007	Nakagawa et al., Rohm ²⁰⁾
(11 $\bar{2}$ 2)	(11 $\bar{2}$ 2) bulk GaN	various QWs structure, both LED and QW structure	EL and PL	2008	Ueda et al., Kyoto Univ. and Nichia ¹⁹⁾
(10 $\bar{1}$ 0)	(10 $\bar{1}$ 0) bulk GaN	3 nm 2 QWs, LD structure	PL and temperature measurement	2008	Kubota et al., Rohm ²¹⁾
(11 $\bar{2}$ 0)	<i>r</i> -Sapphire	2.4 to 7.2 nm 10 QWs (GaN with AlGaN barrier), QW structure	PL	2008	Badcock et al., Univ. Manchester and Univ. Cambridge ²²⁾
(10 $\bar{1}$ 0), (11 $\bar{2}$ 0), (11 $\bar{2}$ 0)	(10 $\bar{1}$ 0) and (11 $\bar{2}$ 0) bulk GaN	3 to 4 nm 8 QWs, LED and QW structure	EL and PL	2010	You et al., RPI ²³⁾
(20 $\bar{2}$ 1)	(20 $\bar{2}$ 1) bulk GaN	3 nm 3 QWs, LD and LED structure	EL	2010	Kyono et al., Sumitomo ²⁴⁾
(10 $\bar{1}$ 0)	(10 $\bar{1}$ 0) bulk GaN	2 to 4 nm 3 QWs, LED structure	EL, with carbon black as absorbing element	2011	Brinkley et al., UCSB ²⁵⁾
(10 $\bar{1}$ 2), (10 $\bar{1}$ 1), (11 $\bar{2}$ 2), (20 $\bar{2}$ 1), (10 $\bar{1}$ 0)	Various bulk GaN	3 nm 3 QWs, QW structure	PL	2011	Schade et al., Fraunhofer Institute for Applied Solid State Physics IAF, Univ. Freiburg, TU Berlin, Leibniz-Institut für Hochstfrequenztechnik ²⁶⁾
(20 $\bar{2}$ 1),	(20 $\bar{2}$ 1) and (20 $\bar{2}$ $\bar{1}$) bulk GaN	3 nm 3 QWs, LED structure	EL	2011	Zhao et al., UCSB ²⁷⁾
(30 $\bar{3}$ 1), (30 $\bar{3}$ $\bar{1}$)	(30 $\bar{3}$ 1) and (30 $\bar{3}$ $\bar{1}$) bulk GaN	3 nm SQW, LED structure	EL	2013	Zhao et al., UCSB ²⁸⁾

2. Physical mechanism

The wurtzite structure is the lowest energy structure for GaN, AlN, and InN. The wurtzite structure has 6mm point symmetry and thus is polar and piezoelectric. When an InGaN QW is coherently grown on GaN, the strain-induced piezoelectric polarization difference and spontaneous polarization difference at the InGaN/GaN interface causes large electric fields in the InGaN QWs which in turn causes electron and hole separation and results in the quantum confined stark effect (QCSE) and an increase the radiative lifetime.³⁻⁵⁾ One way to avoid or reduce the QCSE is to use either a nonpolar (*a*- or *m*-plane) or semipolar plane.⁶⁻⁹⁾ Some studies proposed the use of *c*-plane polarization-matched *c*-plane AlInGaN quaternary barriers between the InGaN QWs to match the polarization charge at AlInGaN/InGaN inter-

faces.³⁹⁾ However, the polarization charge mismatch at the bottom of the first InGaN/GaN QW and at the last barrier between InGaN/GaN still exists and will likely impact the total electric field across the active region of the device and additionally impact carrier transport. Recent efforts in InGaN MQW solar cells showed that modifying the doping profile in the device structure can effectively screen the polarization effects and improve the carrier transport, which means the polarization field in QW influences the carrier transport and recombination significantly.⁴⁰⁾ Takeuchi et al. calculated the dependence of piezoelectric fields on crystal orientations for Ga_{0.9}In_{0.1}N/GaN heterostructures on various planes and showed zero or greatly reduced polarization field can be achieved on nonpolar and semipolar planes.⁴¹⁾ Several other groups have calculated the polarization discontinuity for coherently stressed InGaN/GaN or AlGaN/GaN heterostruc-

Table II. List of theoretical calculations on electronic properties and band structures for III–nitride semiconductors (calculations are mainly on bulk material unless otherwise noted).

Orientations	Structures	Methods	Years	Institutes
<i>c</i> -plane	Wurtzite AlN and GaN	first-principles full-potential linearized augmented plane-wave method within the local-density-functional approximation	1995	Suzuki et al., Matsushita Electric Industrial, Univ. Osaka Prefecture ²⁹⁾
<i>c</i> -plane	Wurtzite AlN, GaN, InN	Kane’s model, $\mathbf{k} \cdot \mathbf{p}$ method	1996	Chuang et al., UIUC ³⁰⁾
<i>c</i> -plane	Wurtzite AlN, GaN, InN	first-principles density functional theory and the linearized augmented plane wave band structure method	1996	Wei et al., Natl. Renewable Energy Lab. ³¹⁾
<i>c</i> -plane	Wurtzite GaN and InN	empirical pseudopotential method	1997	Yeo et al., Natl. Univ. Singapore ³²⁾
<i>c</i> -plane	Wurtzite and Zincblende AlN, GaN, InN	first-principles density functional calculations using both local density approximation and the generalized gradient approximation for the exchange correlation functional	1999	Stampfl et al., Xerox PARC ³³⁾
<i>c</i> -plane	Wurtzite and Zincblende AlN, GaN, InN and their alloys	review article with various calculation methods	2003	Vurgaftman et al., Naval Res. Lab. ³⁴⁾
Arbitrary crystal orientations	Wurtzite InGaN QW	$\mathbf{k} \cdot \mathbf{p}$ method multiband effective-mass theory with an arbitrary crystal orientation	2007	Park et al., Catholic Univ. Daegu, Univ. Seoul, UIUC ^{35,36)}
<i>c</i> -plane	Wurtzite AlN, GaN, InN	first-principles approach based on hybrid-functional density functional theory	2009	Yan et al., UCSB ³⁷⁾
Nonpolar and semipolar planes	Wurtzite InGaN QW with 20% In	$6 \times 6 \mathbf{k} \cdot \mathbf{p}$ Hamiltonian and a self-consistent Schrödinger-Poisson solver	2009	Scheibenzuber et al., Univ. Regensburg, ETH Zurich, Univ. Braunschweig ³⁸⁾

tures.^{41–44)} Below, we will follow the more recent treatment of Romanov, which is based on closed analytical formalism in linear elasticity.⁵⁾ Figure 1 shows the *c*-plane, nonpolar, and frequently used semipolar planes of the wurtzite crystal structure.

To consider the basic properties of nonpolar and semipolar plane, we need to define the two coordinate systems first. When assuming the *c*-axis in the GaN template is inclined at the angle θ with respect to the normal vector of the template’s surface, we use two coordinate systems *xyz* and *x’y’z’* as shown in Fig. 2—these are designated as the N- and P-coordinate systems for the “natural” and “primed” coordinate systems, respectively, as described in detail in Romanov et al.⁵⁾ The natural coordinate *z* is in the direction [0001] of the wurtzite structure, while the two other natural coordinates *x* and *y* are in the basal (0001) plane. For definitiveness and simplicity, we choose the *x*-axis along $[\bar{1}2\bar{1}0]$ [*a*-direction (formally, the $-\mathbf{a}_2$ direction)] and the *z*-axis parallel to [0001] for (*h*0*h*l) planes. In the primed P-coordinate system the *z'*-axis is in the direction of the template’s surface normal, the two other axes *x'* and *y'* are in the template’s surface plane and the *x'*-axis serves as the rotation axis for the *c*-axis inclination.

When the growth plane is inclined from the *c*-plane by an angle θ , the total polarization discontinuity for a coherent layer of In_{*x*}Ga_{1–*x*}N on GaN induced by the anisotropic strain can be calculated based on anisotropic linear elasticity. The $P_{L_z'}^{pz}$ can be calculated by as $P^{pz} \cos \theta$. After straightforward

algebra,⁵⁾ the strain induced piezoelectric polarization, $P_{L_z'}^{pz}$, can be expressed

$$P_{L_z'}^{pz} = e_{31} \cos \theta \epsilon_{x'x'} + \left(e_{31} \cos^3 \theta + \frac{e_{33} - e_{15}}{2} \sin \theta \sin 2\theta \right) \epsilon_{y'y'} + \left(\frac{e_{31} + e_{15}}{2} \sin \theta \sin 2\theta + e_{33} \cos^3 \theta \right) \epsilon_{z'z'} + [(e_{31} - e_{33}) \cos \theta \sin 2\theta + e_{15} \sin \theta \cos 2\theta] \epsilon_{y'z'}, \quad (1)$$

where the elements e_{ij} are the piezoelectric tensor in Voigt notation. The total polarization difference at the InGaN/GaN layer can be calculated by

$$\Delta P_z' = P_{L_z'}^{pz} + (P_L^{sp} - P_S^{sp}) \cos \theta, \quad (2)$$

where P_L^{sp} and P_S^{sp} are the spontaneous polarization of the InGaN layer and the substrate layer, respectively. When combined with known or calculated values of spontaneous polarization, the polarization difference as a function of θ is shown in Fig. 3.⁵⁾

The total polarization discontinuity for a coherently stressed InGaN layer on GaN switches sign for semipolar planes misoriented at angles $\theta \gtrsim 45^\circ$ and is zero for $\theta = 90^\circ$ (which corresponds to the nonpolar *a*- or *m*-plane). In addition to the change in the total polarization discontinuity, the band structure and light emission polarization properties will also be modified due to the anisotropic strain in coherently stressed nonpolar and semipolar heterostructures. To understand the influence of anisotropic strain on the light emission polarization properties in the nonpolar and semi-

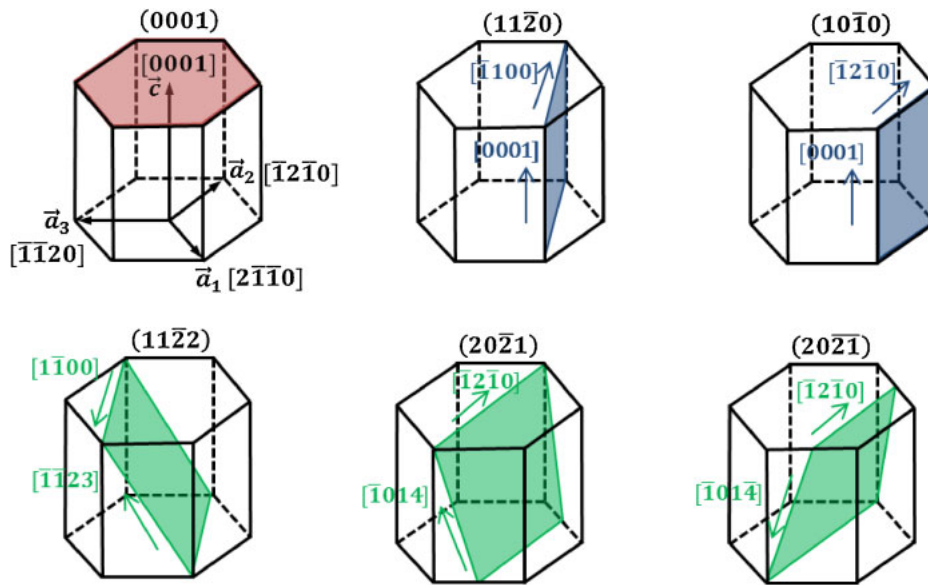


Fig. 1. (Color online) Schematic views of polar, nonpolar and semipolar planes for the wurtzite crystal structure.

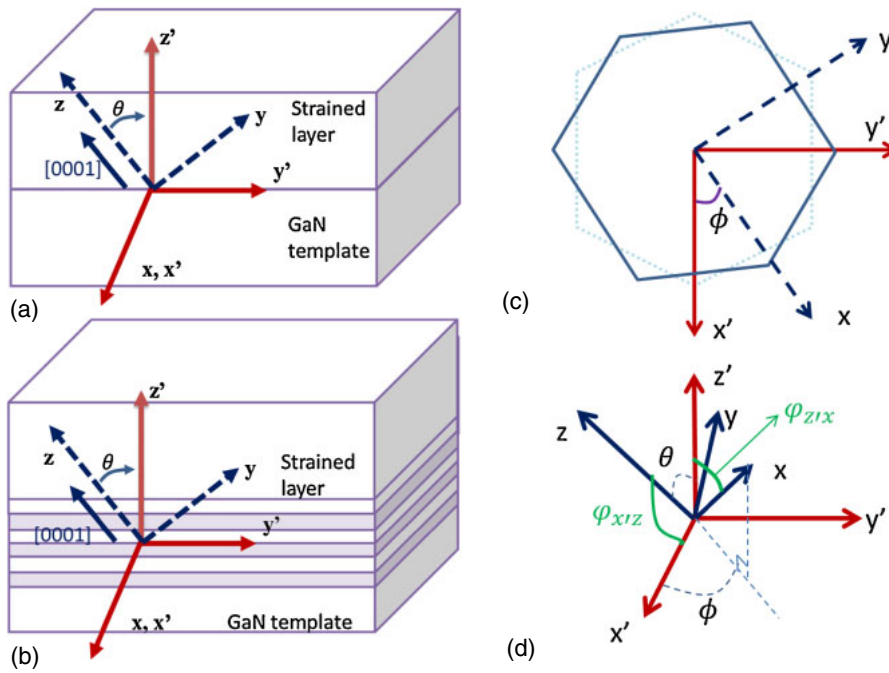


Fig. 2. (Color online) Coordinate systems used in calculations of strain induced polarization: xyz —natural coordinate system associated with c -axis; $x'y'z'$ —coordinate system related to the layer surface normal. (a) Single mismatched layer and (b) multiple QWs.⁵⁾

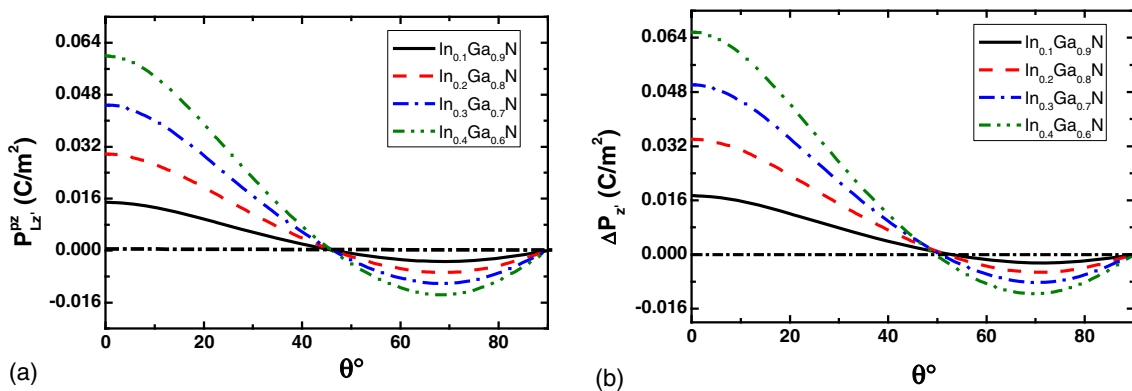


Fig. 3. (Color online) The calculated polarization charge densities as a function of the inclination angles for an InGaN QW.⁵⁾

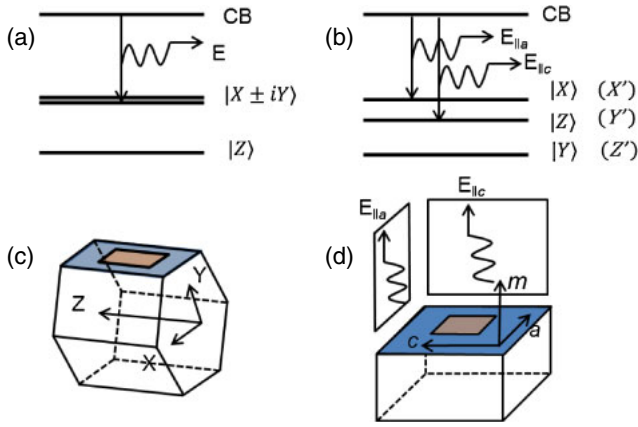


Fig. 4. (Color online) The relative positioning of VBs for (a) polar *c*-plane and (b) nonpolar *m*-plane structures. (c) Schematic of *m*-plane devices in the wurtzite crystal structure. (d) Illustration of the light polarization of an *m*-plane LED.²⁵⁾

polar QWs, we need to consider the following issues: (1) the changes of the VB states mixing due to the anisotropic strain; (2) the energy separation of the first VB (CH1) and the second VB (CH2), and (3) the effective mass differences along the vertical confined direction of CH1 to CH2 bands, which will strongly affect the quantum confinement. For example, if the effective mass of CH1 band along the *z'*-direction (m_z^*) is smaller than the CH2 band, the energy separation of CH1 and CH2 bands will become smaller because the CH1 band will have a larger confinement energy. In fact, the CH2 band might even surpass the CH1 band and become the highest energy band. In addition, more subbands will be formed due to the quantum confinement. On the other hand, if m_z^* is lighter for the CH2 band, the valley separation will become even larger.

Figure 4 presents the relative positioning of VBs for (a) polar *c*-plane and (b) nonpolar *m*-plane structures, where (c) presents the schematic picture of *m*-plane devices in a wurtzite structure and (d) is the light polarization of the *m*-plane LEDs.²⁵⁾ To reiterate, the VB structure of wurtzite GaN is developed from the on the $|X\rangle$, $|Y\rangle$, $|Z\rangle$ states, which correspond to the nitrogen p_x , p_y , and p_z orbitals, respectively. The six band structure bases of the wurtzite structure including spins can be expressed as $|u_1\rangle$ to $|u_6\rangle$ and are $(1/\sqrt{2})|X + iY, \uparrow\rangle$, $(1/\sqrt{2})|X + iY, \downarrow\rangle$, $|Z, \uparrow\rangle$, $|Z, \downarrow\rangle$, $(1/\sqrt{2})|X - iY, \uparrow\rangle$, $(1/\sqrt{2})|X - iY, \downarrow\rangle$, where the polarization of the emission light is strongly affected by these bases. For the *c*-plane structure, the upper two bands are basically $|u_1\rangle$ and $|u_6\rangle$ ($|X \pm iY\rangle$ states), where the $|X\rangle$ and $|Y\rangle$ are equally mixed. Therefore, for conventional *c*-plane structures, the equibiaxial compressive stress for an InGaN layer does not change the separation of the top two VBs $|u_{1,6}\rangle$ and $|u_{2,5}\rangle$ ($|X\rangle$ and $|Y\rangle$ states are moving up equally and the $|Z\rangle$ state is moving down as shown in Fig. 4) so that the polarization of the light for emission normal to the top of the LED chip would be isotropic. The edge emission from *c*-plane LEDs is indeed highly polarized.⁴⁵⁾ However, the polarization of the edge emission did not attract much attention as most LEDs are top emitting devices. For coherent *m*-plane InGaN/GaN heterostructures, the strain component affecting to the $|X\rangle$ and $|Y\rangle$ states becomes unequal. For example, in the nonpolar case where the growth direction is

rotated 90° about *x*-axis as shown in Fig. 2, the original *y*-axis becomes the new *z'*-axis and the *z*-axis rotates to the original *y*-axis.⁵⁾ Therefore, the in plane compressive strain is in the *x*- and *z*-direction and tensile strain is in the *y*-direction. Under this condition, the original $|Y\rangle$ (Z') state will be pulled down and the original $|X\rangle$ (X') and $|Z\rangle$ (Y') states will be pulled up. Therefore, the pure $|X\rangle$ (X') will be the upper band and the light emission will become linearly polarized light as shown in Fig. 4. For *a*-plane InGaN/GaN heterostructures, a similar effect will be observed and the $|Y\rangle$ state would be the upper band for this case. For semipolar planes, the analysis is more complicated because of the shear strains ϵ_{zx} and ϵ_{zy} (expressed in the natural coordinate system). To understand the detailed influence of the strain, the $6 \times 6 \mathbf{k} \cdot \mathbf{p}$ method is usually used to analyze these problems.⁴⁶⁾ The 6×6 Hamiltonian can be expressed as

$$H^v u = \begin{pmatrix} F & 0 & -H^* & 0 & K^* & 0 \\ 0 & G & \Delta & -H^* & 0 & K^* \\ -H & \Delta & \lambda & 0 & I^* & 0 \\ 0 & -H & 0 & \lambda & \Delta & I^* \\ K & 0 & I & \Delta & G & 0 \\ 0 & K & 0 & I & 0 & F \end{pmatrix} \begin{pmatrix} |u_1\rangle \\ |u_2\rangle \\ |u_3\rangle \\ |u_4\rangle \\ |u_5\rangle \\ |u_6\rangle \end{pmatrix}, \quad (3)$$

where

$$\begin{aligned} F &= \Delta_1 + \Delta_2 + \lambda + \theta, \\ G &= \Delta_1 - \Delta_2 + \lambda + \theta, \\ \lambda &= \left(\frac{\hbar^2}{2m_0}\right)[A_1 k_z^2 + A_2(k_x^2 + k_y^2)] + D_1 \epsilon_{zz} + D_2(\epsilon_{xx} + \epsilon_{yy}), \\ \theta &= \frac{\hbar^2}{2m_0}[A_3 k_z^2 + A_4(k_x^2 + k_y^2)] + D_3 \epsilon_{zz} + D_4(\epsilon_{xx} + \epsilon_{yy}), \\ K &= \frac{\hbar^2}{2m_0} A_5(k_x + ik_y)^2 + D_5(\epsilon_{xx} - \epsilon_{yy} + 2i\epsilon_{xy}), \\ H &= \frac{\hbar^2}{2m_0} i[A_6 k_z(k_x + ik_y) + A_7(k_x + ik_y)] + iD_6(\epsilon_{xz} + i\epsilon_{yz}), \\ I &= \frac{\hbar^2}{2m_0} i[A_6 k_z(k_x + ik_y) - A_7(k_x + ik_y)] + iD_6(\epsilon_{xz} + i\epsilon_{yz}), \\ \Delta &= \sqrt{2}\Delta_3, \end{aligned} \quad (4)$$

D_1 – D_6 are the deformation potentials and A_1 – A_7 are the fitting parameters to the VB structure. k_i and ϵ_{ij} ($i, j = x, y, z$) are the wave vector and the strain tensor. Δ_1 is the crystal-field energy and Δ_2 and Δ_3 are the spin–orbit energy parameters. These parameters can be found in Ref. 10. Note that there are many theoretical calculations which provide different values for A_1 to A_7 . Particularly, the deformation potentials D_1 to D_6 are very different from these studies. A brief summary of the theoretical calculations is listed in Table II.^{29–38)}

When the crystal orientation rotates to the primed system, k_x , k_y , and k_z need to be rotated as well. The relation of the new coordinates and the old coordinates can be rotated by the rotation matrix U_{ij} where $U_{x'x} = \cos \varphi_{x'x}$ and is the direction cosine between the x' - and x -axes. Here $\varphi_{x'x}$ is the angle between x' -axis to x -axis as shown in Fig. 2(d). Similarly, $U_{x'z} = \cos \varphi_{x'z}$ and is the direction cosine between the x' - and z -axes, and so on. Note that $U_{x'z} \neq U_{z'x}$ because $U_{z'x} = \cos \varphi_{z'x}$ is the direction cosine between the x - and z' -axes. $\varphi_{x'z}$ and $\varphi_{z'x}$ are labeled in Fig. 2(d). The relation of k to k' can be expressed as

$$k'_i = \sum_{\alpha} U_{i\alpha} k_{\alpha}. \quad (5)$$

If we define ϕ as the angle between the θ rotating axis (x' -axis) to x -axis as shown in Fig. 2(c) and we rotate the coordinates by θ with the rotating axis as defined by Fig. 2. We can derive the rotation matrix U as

$$U = \begin{pmatrix} \cos \phi & -\sin \phi & 0 \\ \cos \theta \sin \phi & \cos \theta \cos \phi & -\sin \theta \\ \sin \theta \sin \phi & \sin \theta \cos \phi & \cos \theta \end{pmatrix}. \quad (6)$$

If x -axis is the rotation axis, then $\phi = 0$, the rotating matrix U becomes

$$U = \begin{pmatrix} 1 & 0 & 0 \\ 0 & \cos \theta & -\sin \theta \\ 0 & \sin \theta & \cos \theta \end{pmatrix}, \quad (7)$$

and

$$\begin{aligned} k'_x &= k_x, \\ k'_y &= \cos \theta k_y - \sin \theta k_z, \\ k'_z &= \sin \theta k_y + \cos \theta k_z, \end{aligned} \quad (8)$$

after replacing the k'_x , k'_y , and k'_z into the 6×6 Hamiltonian. We can solve the Hamiltonian by an eigenvalue solver. If we have confinement in the z' -direction, which is the crystal growth orientation z' -axis, the k'_z will be transformed into the differential form $-i\partial/\partial z'$ and finite difference method can be used to discretize the equation. For the interband transition, the emitting strength for different polarized light is mainly determined by the momentum matrix element

$$|\langle f_e(z') | f_h(z') \rangle|^2 \cdot |\langle s | \hat{a} \cdot (-i\hbar \nabla) | u_i \rangle|^2, \quad (9)$$

where $|\langle f_e(z') | f_h(z') \rangle|$ denotes the overlap between the z' -dependent envelope function of the conduction band (CB) and VB, which decides the dipole strength. \hat{a} is the unit vector indicating the polarization direction of the generated light and $-i\hbar \nabla$ is the momentum operator. $\hat{a} \cdot (-i\hbar \nabla) | u_i \rangle$ determines the emission strength of different polarization light. $\langle s |$ represents the s -like state of the CB electron. However, $| u_i \rangle$ here denotes the original six bases with natural coordinates $| X \rangle$, $| Y \rangle$, and $| Z \rangle$. To calculate light polarization in the new coordinate system, we need to rotate $| u_i \rangle$ to $| u'_i \rangle$ by the rotation matrix U_{ij} again here. For example, in the semipolar plane, if we get the eigenstate of $| u_i \rangle$ to be a mix of $a| X \rangle + b| Y \rangle + c| Z \rangle$, $| X' \rangle$, $| Y' \rangle$, and $| Z' \rangle$ will be given as

$$\begin{aligned} | X' \rangle &= a| X \rangle, \\ | Y' \rangle &= b \cos \theta | Y \rangle - c \sin \theta | Z \rangle, \\ | Z' \rangle &= b \sin \theta | Y \rangle + c \cos \theta | Z \rangle. \end{aligned} \quad (10)$$

Therefore, to get x' - and y' -polarized light strength, which is what is usually measured in the experiment, we take the scalar product of

$$\begin{aligned} \hat{x}' \cdot (-i\hbar \nabla) | u \rangle &= \hat{x}' \cdot (-i\hbar \nabla) | X' \rangle = a | p_x | X \rangle \\ \hat{y}' \cdot (-i\hbar \nabla) | u \rangle &= \hat{y}' \cdot (-i\hbar \nabla) | Y' \rangle \\ &= b \cos \theta | p_y | Y \rangle - c \sin \theta | p_z | Z \rangle \\ \hat{z}' \cdot (-i\hbar \nabla) | u \rangle &= \hat{z}' \cdot (-i\hbar \nabla) | Z' \rangle \\ &= b \sin \theta | p_y | Y \rangle + c \cos \theta | p_z | Z \rangle, \end{aligned} \quad (11)$$

where $p_x = -i\hbar \partial/\partial x$ and due to the symmetric, we can define the momentum matrix element, $|\langle s | p_x | X \rangle| = |\langle s | p_y | Y \rangle| =$

$|\langle s | p_z | Z \rangle| = p_{cv}$. Therefore, the light emission intensity for different polarized light would be

$$\begin{aligned} x'\text{-polarized light} &: \propto |a|^2 p_{cv}^2, \\ y'\text{-polarized light} &: \propto |b \cos \theta - c \sin \theta|^2 p_{cv}^2, \\ z'\text{-polarized light} &: \propto |b \sin \theta + c \cos \theta|^2 p_{cv}^2. \end{aligned} \quad (12)$$

If the state is purely $| Y \rangle$ state after calculation where $b = 1$ and $a = c = 0$, the equation will be simplified to

$$\begin{aligned} y'\text{-polarized light} &: \propto |\cos \theta|^2 p_{cv}^2, \\ z'\text{-polarized light} &: \propto |\sin \theta|^2 p_{cv}^2. \end{aligned} \quad (13)$$

Note that the direction of light propagation will be perpendicular to the direction of light polarization. For light propagating along the y' -direction, y' -polarized light will not contribute any role and the emission strength would be simply proportional to $\sin^2 \theta$. For light propagating along the z' -direction, the light intensity would be proportional to $\cos^2 \theta$. The result would be simply like a dipole source along the y -direction, where the emission strength at the tilt angle θ' from the y -axis is $\sin^2 \theta'$. And the light intensity propagating along the y' -direction would be simply proportional to $\sin^2 \theta$ since $\theta' = \theta$. And the light propagating to the z' -direction would be proportional to $\sin^2(\theta + 90^\circ) = \cos^2 \theta$ since $\theta' = \theta + 90^\circ$. For light polarized in a general direction \hat{a} , determination of the emission strength necessitates the use of Eq. (11) instead of Eq. (12), where the inner product should be done before the square is taken.

Figure 5 shows the calculated $E-k$ relation of the bulk $\text{In}_{0.2}\text{Ga}_{0.8}\text{N}$ material under the same lateral compressive strain in different growth orientations. Note that this result does not reflect the influence of the quantum confined effect but only considers the influence of strain deformation potential. The red, green, and blue (RGB) colors mean the strength of $| X' \rangle$ -, $| Y' \rangle$ -, and $| Z' \rangle$ -like states in the primed system, respectively. If the states are mixed, the color will change to according to the RGB strength. Figure 5(a) shows the $E-k$ relation of the bulk c -plane InGaN material without strain. As we can see at the center of the Γ valley, the top two bands are mixed with $| X \rangle$ and $| Y \rangle$ states, which are usually denoted as $| X \pm iY \rangle$ states, while the $| Z \rangle$ state is the third VB. When the biaxial compressive strain is applied along lateral x - and y -direction and tensile strain in the z - (c -axis) direction, which is shown in Fig. 5(b), the $| X \pm iY \rangle$ states remain as the top two bands since $| X \rangle$ and $| Y \rangle$ states are equally compressed as mentioned earlier. The $| Z \rangle$ state, however, moves to even lower position due to the tensile strain in the z -direction. As a result, the emission will still be mainly dominated by $| X \pm iY \rangle$ where the emission perpendicular to the surface should be isotropic unpolarized light. For the m -plane case as shown in Fig. 5(c), due to the anisotropic strain as discussed earlier, the $| Y \rangle$ state (Z') move down due to the tensile strain, and $| X \rangle$ (X') and $| Z \rangle$ (Y') states move up due to the compressive strain. The top band becomes $| X' \rangle$ state and the light emission will be mainly x' -polarized light, where electric field of the emitted light is parallel to the a -axis. For the semipolar plane case, such as (11 $\bar{2}$ 2) as shown in Fig. 5(d), we need to rotate ϕ by 90° and θ by 58° . Now the y -axis (x' -axis, which is the m -axis) is the rotating axis of θ . Due to the anisotropic strain and the shear strain in the semipolar QW, the x - and z -axis and strain of y -axis (x') remains the same, the top VB will be $| Y \rangle$ (X') state.

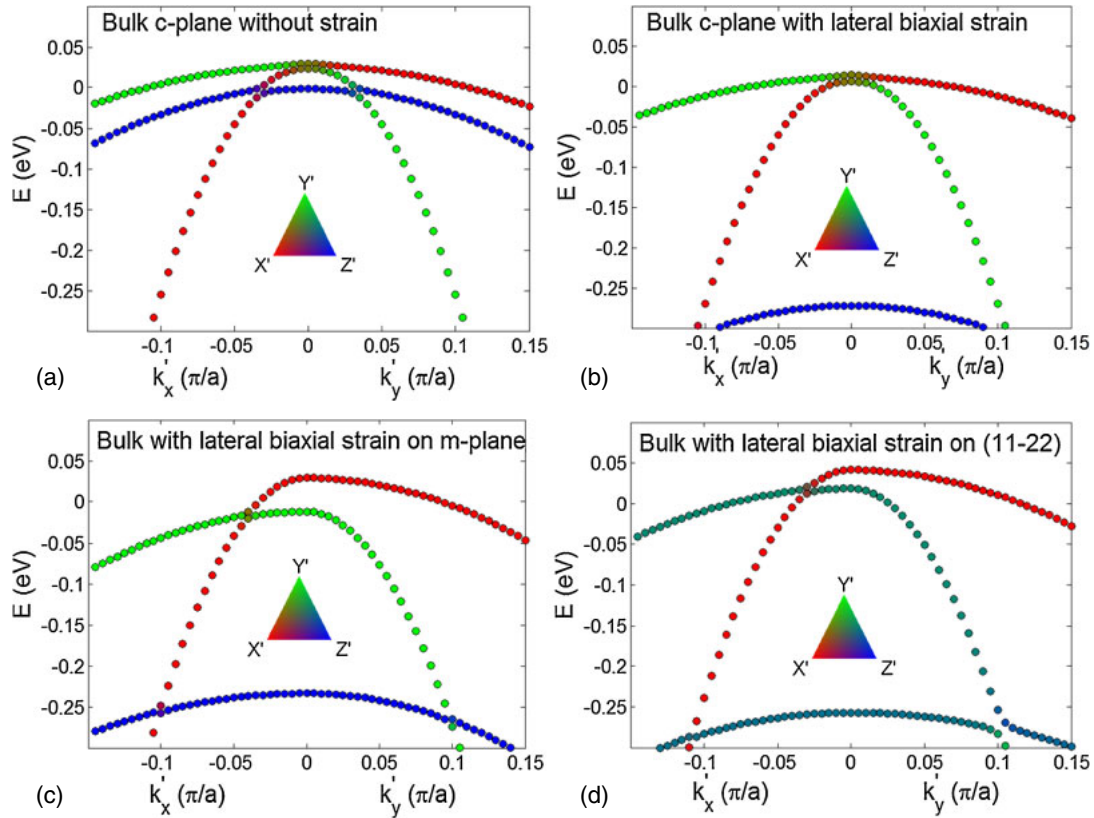


Fig. 5. (Color online) (a) The calculated valence band $E-k$ relationship for bulk c -plane $\text{In}_{0.2}\text{Ga}_{0.8}\text{N}$ without strain. (b)–(d) are the calculated $E-k$ relationship for bulk $\text{In}_{0.2}\text{Ga}_{0.8}\text{N}$ under biaxial strain for the c -plane, m -plane, and $(11\bar{2}2)$ plane, respectively. The RGB color represents the strength of X' , Y' , and Z' states, respectively. Note that for c -plane, $X' = X$, $Y' = Y$, and $Z' = Z$.

But the second and third state are mixed with $|X\rangle$ - and $|Z\rangle$ -like states (Y' and Z') depending on the rotation angle and the strain (or indium composition). If the rotation axis is x -axis (a -axis) such as $(20\bar{2}1)$, the top VB will be mainly $|X\rangle$ (X') state and the second and third states will be mixed with $|Y\rangle$ and $|Z\rangle$ states. The light emission will still be polarized. To realize an accurate estimate of the VB energies for different template orientation angles, especially for QWs, we need to solve the $\mathbf{k} \cdot \mathbf{p}$ equations for each case and include quantum confinement.

In the previous case, the quantum confinement effect was not considered. As mentioned earlier, to accurately model the emission characteristic of InGaN QW we have to consider the quantum confined effect as well. Figure 6 shows the calculated $E-k$ relation for strained c -plane, m -plane, and $(11\bar{2}2)$ InGaN QWs where the quantum confined effect is considered.¹⁰⁾ We find that different subbands are formed due to quantum confinement effects. As shown in Fig. 6(b), for the m -plane case compared to the strained bulk case we see that $|X'\rangle$ forms two subbands if the quantum confined effect is considered. This is because the $|X'\rangle$ band's effective mass along the confined z' -direction, $m_{z'}^*$, is heavier than $|Y'\rangle$ band's effective mass $m_{z'}^*$ so that it can form the first two subbands. Then the $|Y'\rangle$ -state's lower energy subband becomes the third subband. For the $(11\bar{2}2)$ plane which is rotated by $\theta \sim 58.4^\circ$ with respect to the (0001) plane, the first band is still mainly dominated by $|X'\rangle$ -like states at low indium composition ($<30\%$).⁴⁷⁾ The second subband is mixed with $|Y'\rangle$ and $|Z'\rangle$ like mixed states (originally $|X\rangle$ and $|Z\rangle$) as shown in Fig. 6(c). However, as the indium

composition is increased, the $|Y'\rangle$ and $|Z'\rangle$ mixed band will rise to the first band due to the increase of anisotropic strain. This will be discussed later in the experimental section. Therefore, the y' -polarized light intensity will increase and the out-of-plane polarized light, where the light polarization is along the z' -direction will be observed at a tilt angle from z' -axis for the higher indium composition cases.⁴⁷⁾ With the manipulation of the strain, we can estimate the light emission polarization properties for fabricated devices.

In addition, the effective mass in the lateral unconfined region also plays a critical role in band filling. Inside the QW, the freedom of carrier is limited to lateral direction and 2D density of state should be considered. Therefore, the density of states effect mass for a 2D system $m_{\text{DOS},2\text{D}}^*$ should be

$$m_{\text{DOS},2\text{D}}^* = \sqrt{m_x^* m_y^*}. \quad (14)$$

For laser applications, the smaller effective mass will reduce the carrier densities necessary to reach transparency and lower the threshold current densities for lasing. In the nonpolar and semipolar QW system, the $E-k$ relation of the first subband has smaller effective mass than the c -plane cases, which is preferable for lasers. Of course, the waveguide orientation also plays an important role and will be discussed in more detail in Sect. 4.

3. Optical polarization in nonpolar and semipolar LEDs

3.1 Introduction

Polarized optical emission from GaN materials was first

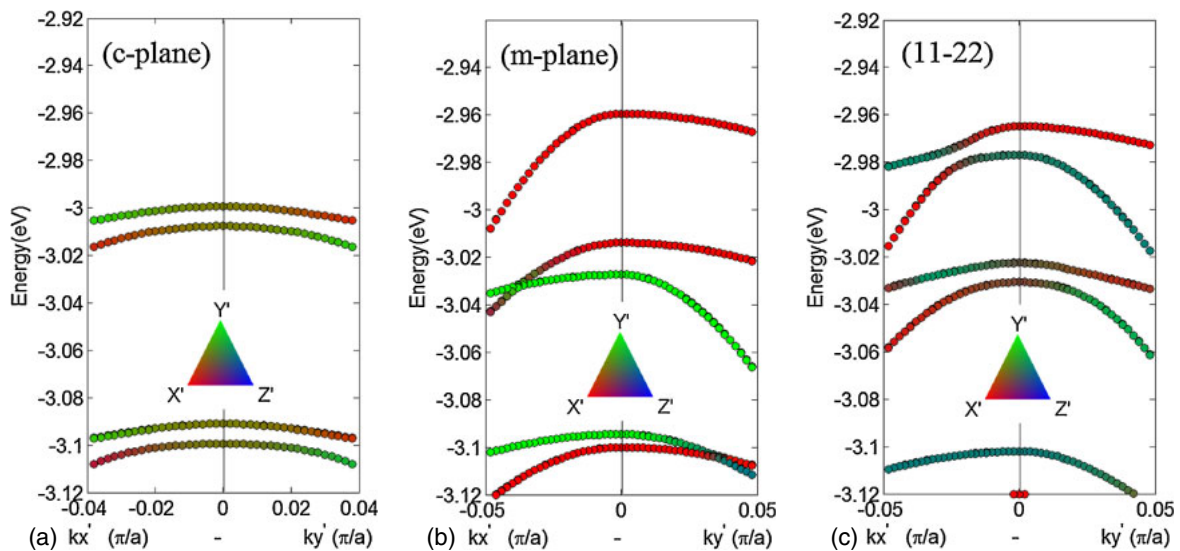


Fig. 6. (Color online) The calculated valence band $E-k$ relationship for c -plane, m -plane, and semipolar plane ($1\bar{1}22$) $\text{In}_{0.2}\text{Ga}_{0.8}\text{N}$ QWs. The zero potential is referred to the CB of GaN. The bandgap of $\text{In}_{0.2}\text{Ga}_{0.8}\text{N}$ is about 2.65 eV.¹⁰⁾

observed by Dingle et al. in 1971, which was considered as a unique characteristic for GaN compared to other common semiconductors.¹¹⁾ The first GaN LEDs demonstrated by Akasaki in 1989, however, were fabricated on conventional c -plane GaN, which does not have polarized emission normal to the c -plane surface.⁴⁸⁾ It was not until the mid-2000s that the experimental efforts on this topic really started to grow due to the successful development of nonpolar and semipolar GaN LEDs.¹²⁻²⁸⁾ Ghosh et al. studied polarization dependence of the absorption, reflectance, and photoreflectance spectra on a compressively strained m -plane GaN film grown on a (0001)-orientated r - LiAlO_2 (γ phase) substrate.¹³⁾ The first reports of polarized electroluminescence were from nonpolar m -plane LEDs, followed by many additional studies for both nonpolar and semipolar devices.⁴⁹⁻⁶⁵⁾ In this section, we will cover several key developments in the topic of polarized optical emission for nonpolar and semipolar LEDs, including devices structures, experimental methods, experimental results, and applications.

3.2 Devices structures and experimental methods

Due to lack of native substrates, early nonpolar and semipolar GaN LEDs were fabricated on foreign substrates, including a -plane GaN templates on r -plane sapphire substrates, m -plane GaN templates on m -plane SiC substrates, and (1122) semipolar GaN templates on m -plane sapphire substrates, etc.^{53,54)} In 2005, Gardner et al. first reported polarized emission from nonpolar m -plane InGaN/GaN LEDs which were grown on m -plane 4H-SiC substrates.¹⁵⁾ However, these early devices showed very low performance due to the high density of extended defects present in the film such as threading dislocations (TDs) ($>10^9 \text{ cm}^{-2}$) and basal-plane stacking faults (BPSFs) ($\sim 10^6 \text{ cm}^{-1}$). In 2006 and 2007, high-quality (TD density $\sim 10^6 \text{ cm}^{-2}$) free-standing nonpolar and semipolar GaN substrates became available due to advancements in hydride vapor phase epitaxy (HVPE) for GaN.⁵⁵⁾ Nonpolar and semipolar GaN substrates with arbitrary orientations were obtained by slicing and polishing from a thick c -plane GaN grown by HVPE. Since then, the progress on

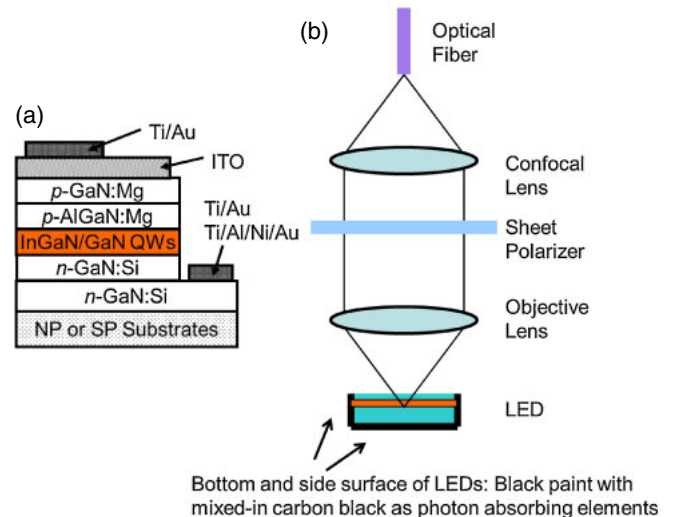


Fig. 7. (Color online) Schematic views of (a) standard nonpolar or semipolar LED structure and (b) the microscope system used for the polarization measurements.^{27,28)} (NP and SP stand for nonpolar and semipolar, respectively).

polarized light emission was very rapid for both nonpolar and semipolar LEDs.

Figure 7(a) presents a schematic figure for a standard LED used in optical polarization measurement.^{27,28)} LEDs are typically grown by metal organic chemical vapor deposition (MOCVD) on free-standing nonpolar and semipolar GaN substrates. The device structure usually consists of a Si-doped n -type GaN layer ($\sim 1 \mu\text{m}$), an active region with single or multiple (typically 2 to 6 periods) InGaN QWs with GaN quantum barriers, a Mg-doped p -type AlGaIn electron blocking layer (EBL), and a Mg-doped p -type GaN layer. The thickness of the InGaN QW typically ranges from 2 to 5 nm. For orientations with very low polarization-related electric field, e.g., nonpolar m -plane or semipolar ($20\bar{2}1$) plane, LED structures with very thick QWs ($>10 \text{ nm}$) can be realized.⁷⁾ For the LED fabrication, a rectangular mesa

pattern is usually formed by lithography and dry etching. An indium tin oxide (ITO) layer is commonly used as current spreading layer, while metal is deposited as contacts and contact pads.

To measure the polarized emission from LEDs, a confocal microscopic system is usually required. This is because of diverging emission of LEDs where reflection and refraction take place. As a result, the measured characteristics contain not only those of inherent light emission but also of stray light that results from scattering, reflection, and refraction at interfaces. For example, early experimental results showed that conventional broad-area techniques, such as optical fibers and Si photodetectors, would lead to lower values of polarization ratio during the measurement.⁵⁶⁾ Figure 7(b) shows a schematic view for a confocal microscopic system used for the LED optical polarization measurement.²⁸⁾ LED emission can be obtained by either electroluminescence (EL) or photoluminescence (PL). An objective lens (20× magnification) with a numerical aperture (NA) of 0.45 was used, where the numerical aperture corresponds to a collection angle of 10° in GaN (27° in air). The depth of field is estimated to be 17 μm in GaN, which is sufficiently smaller than the LED wafer thickness (330 μm). Therefore, reflected light from the backside of the wafer can be eliminated.⁵⁶⁾ For more rigorous measurements, however, photon absorbing elements such as black paint with mixed-in carbon black can be applied to the bottom and side surfaces of individual LEDs to further reduce the scattered light.²⁵⁾ The collected light is collimated by the objective lens and passed through a rotational sheet polarizer before reaching a confocal lens. An optical fiber is used to further couple the light to spectrometers and charge-coupled devices (CCD).

Polarization measurements can be difficult due to scattering-induced depolarization. Taking nonpolar *m*-plane LED as an example, even a small fraction of *a*-polarized light scattered into the *c*-polarization will reduce the observed polarization ratio. It was reported that such scattering was indeed affecting the measurement accuracy despite using a confocal microscope.²⁵⁾ Therefore, special attention is needed for the device preparation and measurement methodology. Brinkley et al. reported that applying black paint with mixed-in carbon black to the bottom and side surface of LEDs as photon absorbing elements can effectively reduce and mitigate the scattering and depolarization effects.²⁵⁾ Consequently, a record high optical polarization ratio was obtained on nonpolar *m*-plane LEDs using improved characterization methods.²⁵⁾

3.3 Nonpolar LEDs

Polarized light emission was first experimentally observed by Gardner et al. using GaN LEDs grown on *m*-plane SiC.¹⁵⁾ A high value of $\rho = 0.81$ and $\Delta E = 49$ meV were obtained from an *m*-plane LED with an emitting wavelength of 492 nm. The study of polarized light emission quickly switched to devices grown on bulk GaN substrates when the substrates became available. Masui et al. observed similar polarized emission on nonpolar LEDs fabrication on *m*-plane bulk GaN substrates with comparable values for ρ and ΔE .⁵⁶⁾ They also studied the effects of substrate miscut angles (0°, 5°, 10°, 27° toward $-c$ -direction) on the optical polarization ratio for *m*-plane LEDs, and found that a ρ value as high as 0.91 can

be obtained on *m*-plane devices with 5° miscut.⁵⁷⁾ In an effort to study the temperature effects on the polarized emission, Nakagawa et al. discovered that the polarization ratios from EL measurement for *m*-plane LEDs increased from 0.85 at 300 K to 0.98 at 100 K.²⁰⁾ They further showed in a PL study for *m*-plane LEDs that the ρ and ΔE increased from 0.71 and 76 meV at a wavelength of 430 nm to 0.92 and 123 meV at 485 nm, indicating a strong dependence of the VB separation on the In composition and strain of the QW.²¹⁾ This was consistent with the theoretical expectations and was further confirmed by studies on green LEDs. For example, You et al. studied optical polarizations for both nonpolar *m*- and *a*-plane LEDs ranging from violet (~400 nm) to green (500 nm) spectral region and reported similar trend for ρ with respect to the emitting wavelength (and In composition).²³⁾ They also found that a higher value of ρ and ΔE for *m*-plane LEDs than *a*-plane devices. More recently, Brinkley et al. reported record high values for the polarization ratio (0.96) for green (520 nm) *m*-plane LEDs by mitigating the internal light scattering and depolarization effect by using absorbing materials on the LED die.²⁵⁾ The ΔE for that device was estimated to be around 125 meV. This multitude of experimental studies also encouraged theoretical work. In a rigorous calculation by Yamaguchi, optical anisotropies for compressively strained nonpolar III-nitride QWs were numerically calculated using the $6 \times 6 \mathbf{k} \cdot \mathbf{p}$ method.⁵⁸⁾ It was discovered that quantum confinement and compressive strain have opposite effects on the anisotropy and that the in-plane polarization degree is determined by the competition of these two effects. Although similar polarization characteristics were predicted for *a*-plane LEDs as for *m*-plane LEDs from theoretical calculations, the majority of the experimental studies have been focused on *m*-plane devices, possibly due to the higher performance of *m*-plane LEDs than *a*-plane devices.

3.4 Semipolar LEDs

Much like nonpolar LEDs, semipolar LEDs should also have intrinsic optical anisotropy due to the low crystal symmetry. Thanks to the development of free-standing semipolar bulk GaN substrates, the progress in optical polarization study on semipolar LEDs has been very rapid. Early work on this topic has been focused on devices grown on semipolar planes with ~60° inclination angle from the *c*-plane, such as the (10 $\bar{1}$ 1) and (11 $\bar{2}$ 2) planes.^{18,57)} In particular, an interesting but counterintuitive phenomenon called polarization switching was observed on (11 $\bar{2}$ 2) LEDs, which was attributed to the crossover of two VBs when the In composition of the QWs reached ~30%.¹⁹⁾ More recently, semipolar planes with higher inclination angles, such as the (20 $\bar{2}$ 1) and (20 $\bar{2}$ 1) planes, attracted significant attention due to the demonstration of high performance green LEDs and low droop blue LEDs.^{27,28)} These “newer” semipolar planes showed several remarkable features, including high indium incorporation rate, low electrical polarization, homogenous atom distributions in the alloys, etc.^{57–62)}

3.4.1 Semipolar (11 $\bar{2}$ 2) LEDs and polarization switching phenomenon

Among the various semipolar planes, the (11 $\bar{2}$ 2) plane first attracted attention due to the high indium incorporation which was advantageous for fabricating long wavelength (>500 nm) devices. Funato et al. demonstrated

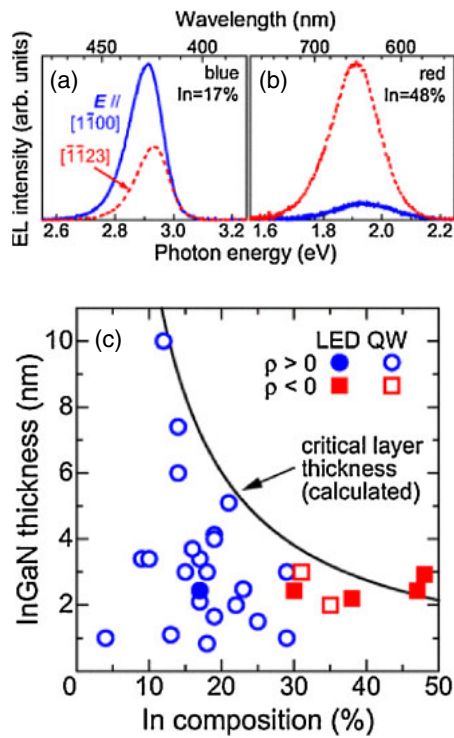


Fig. 8. (Color online) The typical polarization EL spectra of (a) blue and (b) red (112̄2) LEDs and (c) the dependence of ρ on In composition and layer thickness for (112̄2) InGaN QWs.¹⁹⁾

high efficiency LED operation in the blue, green, and amber spectral regions.¹⁸⁾ Their initial study showed that the optical emission from (112̄2) LEDs was polarized along [1100] and [1123] directions, with the former direction as the stronger component [ρ is defined as $\rho = (I_{[1100]} - I_{[1123]}) / (I_{[1100]} + I_{[1123]})$ for the (112̄2) LEDs¹⁹⁾]. However, the LEDs reported by Funato et al. showed very low degree of polarization compared to other nonpolar and semipolar LEDs, with only $\rho = 0.2$ for green LEDs and $\rho = 0.14$ for amber LEDs. Furthermore, the experimental findings did not agree with previous theoretical considerations where ρ generally increased with increasing wavelength (In composition) of the QW. It was later discovered by Ueda et al. that when the In composition of the (112̄2) QW reached $\sim 30\%$, a polarization switch would take place where the emission polarized along [1123] direction would become dominant component.¹⁹⁾ Figures 8(a) and 8(b) show the typical polarization EL spectra of (112̄2) blue and red LEDs, while Fig. 8(c) shows the dependence of ρ on In content and layer thickness of the InGaN QWs.¹⁹⁾ For blue LEDs, ρ showed a positive sign, indicating that the direction of the dominant polarization is perpendicular to the [1123] direction, which was consistent with other results. For red LEDs, however, the polarization switched and a negative ρ was obtained.

These experimental observations initiated considerable efforts to theoretically interpret the polarization switching phenomenon. Ueda et al. proposed that the polarization switch can be explained by the following mechanism, which is illustrated in Figs. 9(a) and 9(b).¹⁹⁾ When the In composition of the InGaN QW is less than than $\sim 30\%$, the topmost VB (denoted as |X>) corresponded to emission from a dipole along the [1100] direction, and the second highest

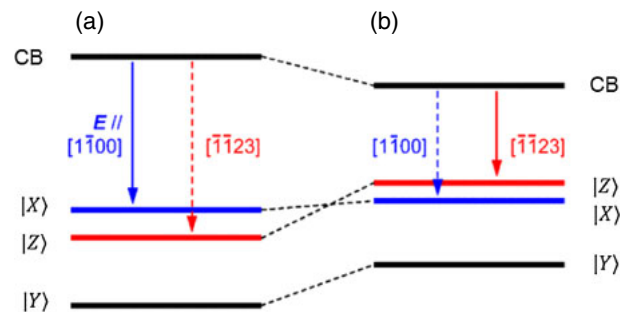


Fig. 9. (Color online) Schematic of band alignments of (112̄2) QWs with (a) In < 30% and (b) In > 30%.¹⁹⁾

VB (denoted as |Z>) corresponded to emission from a dipole along the [1123] direction. When the In composition increased beyond $\sim 30\%$, the |X) and |Z) bands approached one another and eventually a crossover occurred (Note that N-coordinate system used here). As a result, the topmost VB (denoted as |Z)) corresponded to emission from a dipole along the [1123] direction and the second highest VB (denoted as |X)) corresponded to emission from a dipole along the [1100] direction. However, this explanation could not be reproduced by the theoretical calculations using the $k \cdot p$ method. Yan et al. studied the effects of strain on the VB structure for (112̄2) InGaN QWs and found that pseudomorphic strain conditions did not lead to polarization switching with increasing In concentration.⁶³⁾ More recently, Schade et al. extended the polarization switching study to other semipolar QWs, including (1012), (1011), (2021), etc.²⁶⁾ For a given In composition, polarization switching would happen for semipolar planes with inclination angles (with respect to *c*-plane) that are smaller than the critical angle θ_c . For example, at an In composition of 20 to 25%, $\theta_c = 58.4^\circ$, which is close to the inclination angle of the (112̄2) plane. At an In composition of 30 to 35%, $\theta_c = 62^\circ$, which is close to that of the (1011) plane. According to their model, the critical angle reached a maximum value of $\theta_{c,max} = 69.4^\circ$ for bulk calculation of fully stained InN on GaN. Semipolar planes with an inclination angles higher than 69.4° , such as the (2021) plane (75°), would not be affected by the polarization switching effect due to the low shear strain contribution to the valence band energy shift.

3.4.2 Semipolar (202̄1) and (202̄1) LEDs One of the biggest achievements for semipolar GaN research so far was the demonstration of high performance green LEDs and LEDs using the (202̄1) plane.^{59,60)} In 2009, Enya et al. achieved the world's first direct emission true green LD grown on the (202̄1) plane.⁵⁹⁾ Soon after that, Yamamoto et al. showed green (202̄1) LEDs with a high peak external quantum efficiency of 20% and output power of 9.9 mW at 20 mA.⁶⁰⁾ These great successes in device performance quickly led to research on the optical polarization of (202̄1) devices. Kyono et al. and Chung et al. studied the optical polarization for (202̄1) QWs and obtained low values for ρ in the range of 0.2 to 0.4, which was significantly lower than the nonpolar *m*-plane results and also contrary to theoretical expectations.^{24,64)}

In 2011 the semipolar (202̄1) plane, which corresponds to the backside of (202̄1) plane due to the symmetry of

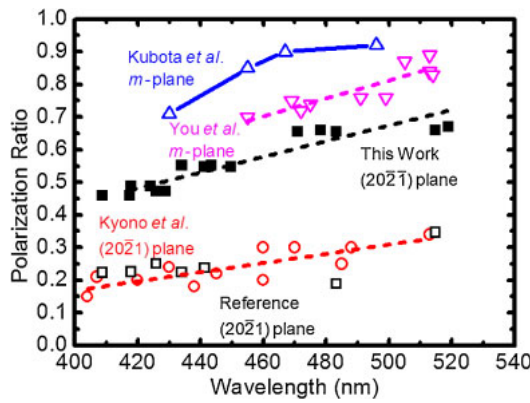


Fig. 10. (Color online) The optical polarization ratios for various nonpolar and semipolar LEDs as a function of the peak wavelength of the dominant component.²⁷⁾

the wurtzite crystal, emerged as a promising new plane with many advantageous properties: high indium incorporation, low electrical polarization, small wavelength shift, and narrow spectrum linewidth.^{61,62)} The polarization-related electric field and the p - n junction built-in electric field were in opposite direction and nearly cancelled each other, which resulted in a relatively flat QW potential profile during device operation.⁶¹⁾ This feature has been used to produce high-efficiency and low-droop blue LEDs with relatively thick (~ 12 nm) QWs.⁷⁾ Zhao et al. studied optical polarization ratio properties for $(20\bar{2}\bar{1})$ LEDs.²⁷⁾ Figure 10 summarizes the optical polarization ratios for various nonpolar and semipolar LEDs as a function of the peak wavelengths of the dominant component.²⁷⁾ The $(20\bar{2}\bar{1})$ LEDs showed a very high value for ρ , which was close to the previous results on m -plane devices. ρ increased with increasing wavelength (In composition), which is also consistent with expectations. On the contrary, the $(20\bar{2}\bar{1})$ LEDs showed very low value for ρ . In addition, the energy separation of the top two valence bands ΔE was extracted from the peak wavelengths of the polarization study and compared with theoretical calculations (shown in Fig. 11).²⁷⁾ The calculation predicted identical ΔE for $(20\bar{2}\bar{1})$ and $(20\bar{2}\bar{1})$ plane, as expected. While the data obtained for ΔE for the $(20\bar{2}\bar{1})$ plane is in reasonable agreement with the calculations, the data obtained for ΔE for the $(20\bar{2}\bar{1})$ plane is significantly smaller than the calculations. A high value for ΔE is preferable for LED and LD performance. In a recent effort to understand the low polarization on $(20\bar{2}\bar{1})$ devices, experimental as well as theoretical work were carried out on LEDs on the $(30\bar{3}\bar{1})$ and $(30\bar{3}\bar{1})$ planes, which were pair of semipolar planes with similar but even higher inclination angle (80° with respect to the c -plane) than the $\{20\bar{2}\bar{1}\}$ planes.²⁸⁾ The study showed identical polarization results for both planes, which were consistent with calculations. The reason for low optical polarization on $(20\bar{2}\bar{1})$ plane is therefore still under investigation.

3.5 Applications

Significant power savings can be achieved by using highly polarized nonpolar and semipolar LED sources as it greatly reduces light generation in the unwanted polarization state. Masui et al. demonstrated a liquid-crystal display (LCD) unit using polarized m -plane LEDs and found that employ-

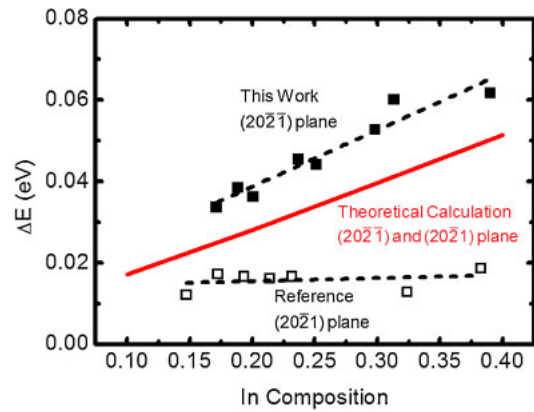


Fig. 11. (Color online) The energy separation ΔE between the top two VBs at the Γ point for 3 nm $(20\bar{2}\bar{1})$ semipolar InGaN QW strained on GaN with different In compositions obtained by the $k \cdot p$ method using NEXTNANO3 software. The experimental data for $(20\bar{2}\bar{1})$ and $(20\bar{2}\bar{1})$ QWs are also plotted for comparison.²⁷⁾

ment of polarized light sources in LCDs indeed contributed to energy savings.⁶⁵⁾ Furthermore, You et al. calculated the overall system efficiency enhancement factor $\xi = 1 + 1/\rho$ for a LCD system using polarized light sources.²³⁾ An equivalent amount of linearly polarized light from an m -plane LED with $\rho = 0.77$ can be achieved with $1/\xi = 44\%$ less source power than an equivalent amount of linearly polarized light from unpolarized light source.

4. Optical polarization in nonpolar and semipolar III-nitride LDs

Much like nonpolar and semipolar III-nitride LEDs, nonpolar and semipolar LDs also exhibit polarized light emission. Unlike the polarized emission from LEDs, though, which is usually measured perpendicular to the growth plane and depends primarily on band structure, the polarized emission from LDs also depends on waveguide orientation and the natural birefringence of III-nitride materials. In this section, we will discuss the characteristics of polarized light emission in nonpolar edge-emitting LDs, semipolar edge-emitting LDs, and nonpolar vertical-cavity surface-emitting lasers (VCSELs).

4.1 Birefringence

A working knowledge of birefringence is essential for understanding the nature of polarized light emission in nonpolar and semipolar LDs. In a birefringent crystal two mutually orthogonal plane polarized waves may be propagated along a common wave normal where the wave normal is perpendicular to the direction of polarization of both of the plane waves.⁶⁶⁾ The indices of refraction of the two waves, which depend on their common wave normal, can be obtained by constructing an ellipsoid known as the *indicatrix*. The indicatrix is defined by the equation

$$\frac{x_1^2}{n_1^2} + \frac{x_2^2}{n_2^2} + \frac{x_3^2}{n_3^2} = 1, \quad (15)$$

where x_1, x_2, x_3 are the *principal axes* of the dielectric constant tensor, K_1, K_2, K_3 are the *principal dielectric constants*, and $n_1 = \sqrt{K_1}$, $n_2 = \sqrt{K_2}$, $n_3 = \sqrt{K_3}$, are the *principal indices of refraction*. If a line is drawn parallel

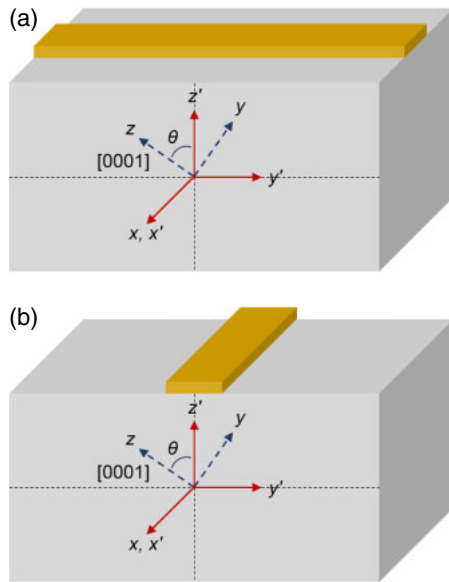


Fig. 12. (Color online) Schematic illustrating how waveguides can be oriented (a) parallel or (b) perpendicular to the y' -direction on a general nonpolar or semipolar plane.

to the common wave normal, the central section of the indicatrix perpendicular to the line will form an ellipse. The two plane polarized waves will have indices of refraction equal to the semi-axes of the ellipse and will be polarized along the semi-axes of the ellipse.⁶⁶⁾ Thus, this construction defines the allowed polarizations and relative phase velocities of two plane waves with a common wave normal in a birefringent crystal (e.g., see Fig. 12 in Ref. 66).

For materials with a hexagonal crystal structure like GaN the indicatrix is an ellipsoid of revolution about the principal symmetry axis or [0001] c -axis. With x_3 as the principal symmetry axis Eq. (15) can be written as

$$\frac{x_1^2}{n_o^2} + \frac{x_2^2}{n_o^2} + \frac{x_3^2}{n_e^2} = 1, \quad (16)$$

where n_o and n_e are called the *ordinary* and *extraordinary* indices of refraction, respectively. The central section of the indicatrix perpendicular to the principal symmetry axis is a circle of radius n_o . Only waves with a wave normal along the principal symmetry axis lack birefringence. Thus, the principal symmetry axis is referred to as the *optic axis* and the crystal is said to be *uniaxial*.⁶⁶⁾

4.2 Waveguide orientation

GaN exhibits uniaxial birefringence with $\Delta n = n_e - n_o \approx 0.011n_o$.⁶⁷⁾ In nonpolar and semipolar LDs, the c -axis is not parallel to all waveguide orientations, so the effects of birefringence have to be considered. In general, it is necessary to distinguish between two possible waveguide orientations in nonpolar and semipolar LDs. These two waveguide orientations are illustrated for a general nonpolar or semipolar plane in Fig. 12. The waveguides can be oriented either parallel or perpendicular to the y' -direction, defined as the *projection of the c -axis* onto the QW plane.

Although the indicatrix construction is very accurate for predicting the polarization of waves in bulk III-nitride crystals, additional factors must be included for predicting the

polarization of modes in multilayer III-nitride waveguides. This difference in accuracy arises from variations in the index of refraction between adjacent layers in III-nitride waveguides and the necessity to match boundary conditions between these layers. Nevertheless, the change in polarization between adjacent layers in a III-nitride waveguide (typically a couple of degrees at most) is still very close to the polarization predicted by the indicatrix construction for waves in a bulk III-nitride crystal, as predicted by theoretical calculations^{38,68)} and confirmed by experimental measurements.^{69,70)} The polarization of modes in a birefringent waveguide is often different than the usual polarization parallel (transverse electric or TE mode) and perpendicular (transverse magnetic or TM mode) to the growth plane, as discussed in more detail below.

For waveguides on nonpolar growth planes, the mirror facets of both waveguide orientations coincide with a natural crystal faces (usually either a - or m -planes), so mirror facets can be formed on both waveguide orientations by cleaving.⁷¹⁾ Conversely, for waveguides on semipolar growth planes, waveguide orientations perpendicular to the y' -direction coincide with natural crystal faces (usually either a - or m -planes), so mirror facets can also be formed on these waveguide orientations by cleaving.⁷¹⁾ However, for waveguides on semipolar growth planes, waveguide orientations parallel to the y' -direction do not coincide with natural crystal faces (i.e., crystal planes with rational Miller indices), so mirror facets need to be formed on these waveguide orientations by dry etching or polishing.⁷²⁾ As cleaving is a more mature technology for fabricating mirror facets than dry etching or polishing, there have been many studies to assess the suitability of waveguide orientations perpendicular to the y' -direction for semipolar LDs,^{19,24,38,68-70,73-75)} as discussed in more detail in Sect. 4.5.

4.3 Relationship between optical gain, birefringence, and waveguide orientation

The unbalanced biaxial stress in nonpolar and semipolar InGaN QWs has been predicted to lead to an increase in optical gain compared to c -plane QWs.³⁸⁾ To understand the relationship between gain, birefringence, and waveguide orientation, it is necessary to consider the various terms in the expression for gain. The expression for gain for two states separated in energy by $E_{21} = E_2 - E_1$ is

$$g_{21} \propto |M_T(E_{21}, \hat{a})|^2 \rho_r(E_{21})(f_2 - f_1), \quad (17)$$

where state 2 is an electron state in the CB, state 1 is hole state in the VB, $|M_T(E_{21}, \hat{a})|^2$ is the square of the momentum matrix element for a transition between states 2 and 1, $\rho_r(E_{21})$ is the reduced density of states for a transition between states 2 and 1, and f_2 and f_1 are the Fermi occupation probabilities of states 2 and 1, respectively.^{76,77)}

The dependence of gain on birefringence and waveguide orientation is determined by the momentum matrix element, which is given by Eq. (9). The square of the wavefunction overlap integral, $|\langle f_e(z') | f_h(z') \rangle|^2$, depends on the crystallographic orientation and is generally larger for nonpolar and semipolar QWs than for c -plane QWs.⁴¹⁾ The other term in the momentum matrix element,

$$|\langle s | \hat{a} \cdot (-i\hbar\nabla) | u_i \rangle|^2, \quad (18)$$

determines the optical polarization and depends on the symmetry of the CB and VB basis states as well as the allowed polarizations of the waveguide. As indicated by Eq. (11), the gain is dependent on the square of the scalar product of \hat{a} and $(-i\hbar\nabla)|u_i\rangle$. Thus, if α is the angle between \hat{a} and $(-i\hbar\nabla)|u_i\rangle$, then the magnitude of the gain should vary as $\cos^2\alpha$.⁷⁰

4.4 Nonpolar III-nitride edge-emitting LDs

Waveguide orientation determines the magnitude of the gain and the polarization of stimulated emission for nonpolar III-nitride edge-emitting LDs. As an example, waveguide orientation is examined below for an *m*-plane III-nitride edge-emitting LD, although the discussion could be generalized to *a*-plane III-nitride edge-emitting LDs as well. According to the indicatrix construction, the allowed polarizations of modes in a waveguide orientated parallel to the *c*-axis are parallel to the *a*-axis (the ordinary axis) and parallel to the *m*-axis (the other ordinary axis), which are parallel to the usual TE and TM modes, respectively. The TE mode couples to emission from the CH1 band ($\cos^2\alpha = 1$) and the TM mode couples to emission from the CH3 band ($\cos^2\alpha = 1$).^{70,78} However, stimulated emission is dominated by the TE mode because of the much higher hole population in the CH1 band than the CH3 band, as confirmed by experimental measurements.^{69,79} Finally, emission from the CH2 band does not couple to either of the waveguide modes because $\cos^2\alpha = 0$ for a waveguide oriented along the *c*-axis.

Also according to the indicatrix construction, the allowed polarization of modes in a waveguide orientated perpendicular to the *c*-axis are parallel to the *c*-axis (the extraordinary axis) and parallel to the *m*-axis (the ordinary axis), which are parallel to the usual TE and TM modes, respectively. The TE mode couples to emission from the CH2 band ($\cos^2\alpha = 1$) and the TM mode couples to emission from the CH3 band ($\cos^2\alpha = 1$).^{70,78} However, stimulated emission is dominated by the TE mode because of the much higher hole population in the CH2 band than the CH3 band, as confirmed by experimental measurements.^{69,79} Finally, emission from the CH1 band does not couple to either of the waveguide modes because $\cos^2\alpha = 0$ for a waveguide oriented perpendicular to the *c*-axis.^{70,78}

Gain is expected to be higher in a waveguide oriented parallel to the *c*-axis than a waveguide oriented perpendicular to the *c*-axis because of the much higher hole population in the CH1 band than the CH2 band. This is confirmed by theoretical calculations³⁸ and experimental measurements.⁷⁹ Figures 13(a) and 13(b) present calculations of material gain for 3 nm nonpolar $\text{In}_{0.2}\text{Ga}_{0.8}\text{N}$ QWs with waveguides oriented parallel and perpendicular to the *c*-axis, respectively.³⁸ For both waveguide orientations the gain is much higher for the TE mode than for the TM mode, as expected from the above analysis of the momentum matrix elements. In addition, the peak gain is several times higher for a given carrier density for the waveguide oriented parallel to the *c*-axis than for the waveguide oriented perpendicular to the *c*-axis, which can be attributed to the much higher hole population in the CH1 band than the CH2 band.

Experimental measurements of *m*-plane LDs with QWs emitting at wavelength of ~ 400 nm (Fig. 14) indicate that the threshold current density is nearly twice as high for ridge

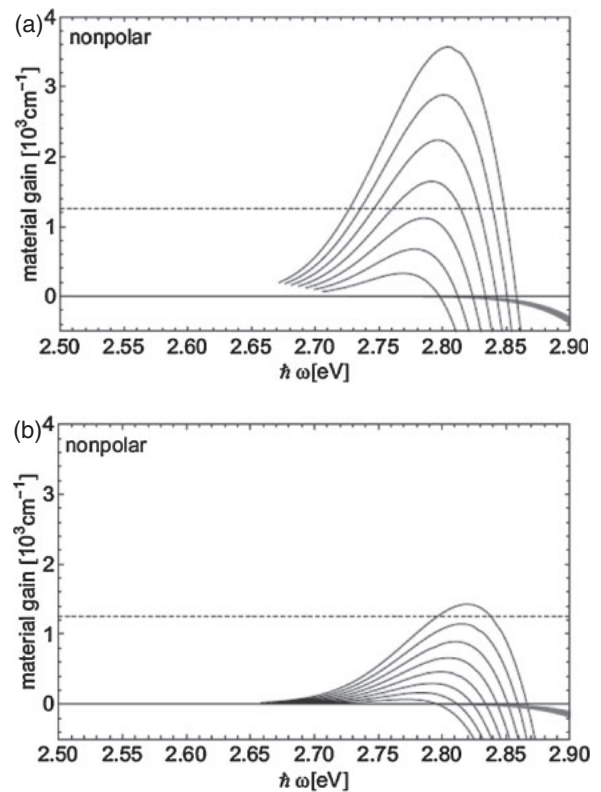


Fig. 13. (a) Material gain for TE mode (black curves) and TM mode (gray curves) of nonpolar QWs with waveguides oriented parallel to the *c*-axis. Estimated threshold gain is indicated as a dashed line. Sheet carrier densities are 3×10^{12} – $6 \times 10^{12} \text{ cm}^{-2}$ in steps of $0.5 \times 10^{12} \text{ cm}^{-2}$. (b) Material gain for TE mode (black curves) and TM mode (gray curves) of nonpolar QWs with waveguides oriented perpendicular to the *c*-axis. Estimated threshold gain is indicated as a dashed line. Sheet carrier densities are 4×10^{12} – $7.5 \times 10^{12} \text{ cm}^{-2}$ in steps of $0.5 \times 10^{12} \text{ cm}^{-2}$.³⁸

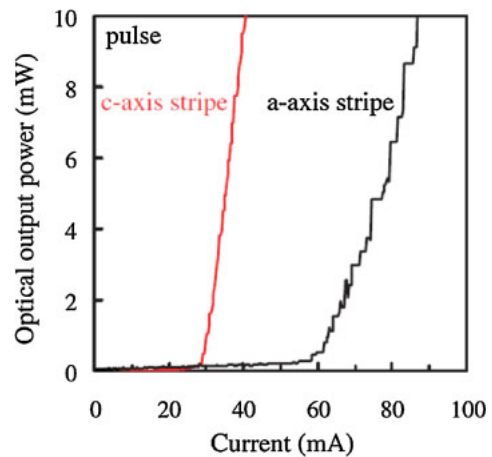


Fig. 14. (Color online) *L*–*I* characteristics of *m*-plane III-nitride LDs with ridge waveguides oriented parallel to either the *c*-axis or the *a*-axis.⁷⁹

waveguide LDs oriented parallel to the *a*-axis than ridge waveguide LDs oriented parallel to the *c*-axis,⁷⁹ in agreement with the theoretical calculations discussed above.³⁸ Finally, for waveguides on *m*-plane LDs, the mirror facets of both waveguide orientations coincide with a crystal face, so mirror facets can be formed on both waveguide orientations by cleaving.⁷¹ However, since the gain is higher for a waveguide oriented parallel to the *c*-axis and *c*-plane mirror facets

can be formed by cleaving, it is clearly advantageous to orient waveguides for m -plane LDs parallel to the c -axis.

4.5 Semipolar III-nitride edge-emitting LDs

Much like nonpolar III-nitride edge-emitting LDs, waveguide orientation determines the magnitude of the gain and the polarization of stimulated emission for semipolar III-nitride edge-emitting LDs. As an example, waveguide orientation is examined below for a $(11\bar{2}2)$ III-nitride edge-emitting LD, although the discussion could be generalized to any semipolar III-nitride edge-emitting LD orientation as well. According to the indicatrix construction, the allowed polarizations of modes in a waveguide orientated parallel to the y' -direction (the $[\bar{1}\bar{1}23]$ direction) are parallel to the m -axis (the ordinary axis) and perpendicular to the $(11\bar{2}2)$ plane, which are parallel to the usual TE and TM modes, respectively. The TE mode couples primarily to emission from the CH1 band ($\cos^2\alpha \approx 1$) and the TM mode couples primarily to emission from the CH3 band ($\cos^2\alpha \approx 1$).^{70,78} Stimulated emission is dominated by the TE mode because of the much higher hole population in the CH1 band than the CH3 band, as confirmed by experimental measurements.^{69,70} Finally, emission from the CH2 band has minimal coupling to both of the waveguide modes because $\cos^2\alpha \approx 0$ for a waveguide oriented along the y' -direction.^{70,78}

Also according to the indicatrix construction, the allowed polarizations of modes in a waveguide orientated perpendicular to the y' -direction are parallel to the c -axis (the extraordinary axis) and parallel to the a -axis (the ordinary axis), which are not aligned with the $(11\bar{2}2)$ plane or its normal and are referred to below as the *extraordinary mode* and the *ordinary mode*, respectively. Both the extraordinary mode and the ordinary mode couple primarily to emission from the CH2 band and the magnitude of the coupling depends on the angle between \hat{a} and $(-i\hbar\nabla)|u_i\rangle$.⁷⁰ Since the c -axis is inclined 58° to the $(11\bar{2}2)$ plane, the angle between \hat{a} and $(-i\hbar\nabla)|u_i\rangle$ is 32° for the extraordinary mode and 58° for the ordinary mode. Therefore, the extraordinary mode is expected to have a reduction in material gain by a factor of $\cos^2 32^\circ \approx 0.7$ and the ordinary mode is expected to have a reduction in material gain by a factor of $\cos^2 58^\circ \approx 0.3$. Thus, both modes experience a reduction in gain due to the nature of the birefringence of a waveguide orientated perpendicular to the y' -direction. Both the extraordinary mode and the ordinary mode also couple to emission from the CH3 band, but the stimulated emission is dominated by emission from the CH2 band because of the much higher hole population in the CH2 band than the CH3 band. Finally, emission from the CH1 has minimal coupling to both of the waveguide modes because $\cos^2\alpha \approx 0$ for a waveguide oriented perpendicular to the y' -direction.

Gain is expected to be higher in a waveguide oriented parallel to the y' -direction than a waveguide oriented perpendicular to the y' -direction (at least for $\text{In}_x\text{Ga}_{1-x}\text{N}$ QWs where x is less than ~ 0.30) because of the higher hole population in the CH1 band than the CH2 band and the $\cos^2\alpha$ dependence of the momentum matrix elements. This is confirmed by theoretical calculations³⁸ and experimental measurements.^{69,70} Figures 15(a) and 15(b) present calculations of material gain for 3 nm $(11\bar{2}2)$ $\text{In}_{0.2}\text{Ga}_{0.8}\text{N}$ QWs with waveguides oriented parallel and perpendicular to the

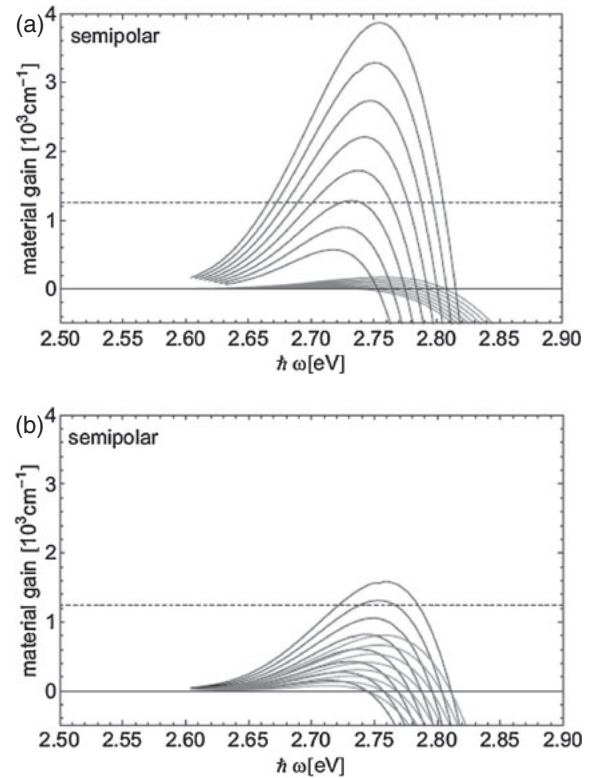


Fig. 15. (a) Material gain for TE mode (black curves) and TM mode (gray curves) of $(11\bar{2}2)$ QWs with waveguides oriented parallel to the y' -direction. Estimated threshold gain is indicated as a dashed line. Sheet carrier densities are 4×10^{12} – $7.5 \times 10^{12} \text{ cm}^{-2}$ in steps of $0.5 \times 10^{12} \text{ cm}^{-2}$. (b) Material gain for extraordinary mode (black curves) and ordinary mode (gray curves) of $(11\bar{2}2)$ QWs with waveguides oriented perpendicular to the y' -direction. Estimated threshold gain is indicated as a dashed line. Sheet carrier densities are 4×10^{12} – $7.5 \times 10^{12} \text{ cm}^{-2}$ in steps of $0.5 \times 10^{12} \text{ cm}^{-2}$.³⁸

y' -direction, respectively.³⁸ For the waveguide orientated parallel to the y' -direction the gain is much higher for the TE mode than for the TM mode, as expected from the higher hole population in the CH1 band than the CH3 band. Similarly, for the waveguide orientated perpendicular to the y' -direction the gain is much higher for the extraordinary mode than for the ordinary mode, as expected from the above analysis of the momentum matrix elements. In addition, the peak gain is several times higher for a given carrier density for the waveguide oriented parallel to the y' -direction than for the waveguide oriented perpendicular to the y' -direction, which can be attributed to the much higher hole population in the CH1 band than the CH2 band and the $\cos^2\alpha$ dependence of the momentum matrix elements.

Experimental measurements of optically pumped $(11\bar{2}2)$ laser structures with a single 6 nm $\text{In}_{0.08}\text{Ga}_{0.92}\text{N}$ QW indicate that the amplified spontaneous emission (ASE) threshold power density [Fig. 16(b)] is about 70% higher for laser stripes oriented parallel to the y' -direction than laser stripes oriented perpendicular to the y' -direction,⁷⁰ in agreement with the theoretical calculations discussed above.³⁸ In addition, measurements of the optical polarization [Fig. 16(a)] indicate that stimulated emission in the waveguide oriented parallel (perpendicular) to the y' -direction was polarized along to the m -axis (c -axis),⁷⁰ as expected from the above analysis of the momentum matrix elements.

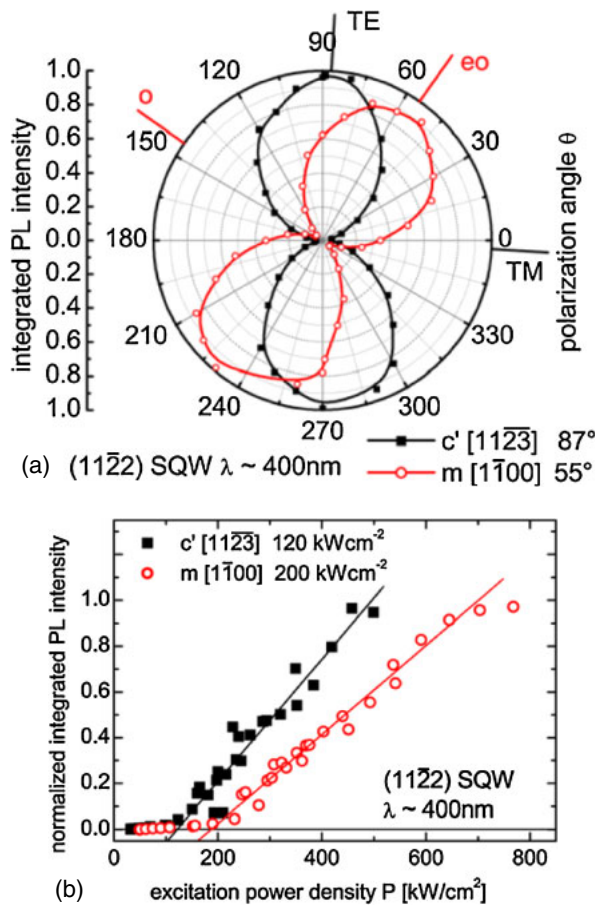


Fig. 16. (Color online) (a) Polarization of the waveguide modes above ASE threshold and (b) dependence of normalized integrated PL intensity on excitation power density for excitation stripes orientated parallel ([11 $\bar{2}$ 3] direction) and perpendicular ([10 $\bar{1}$ 0] m -axis) to the y' -direction on the (11 $\bar{2}$ 2) plane.⁷⁰⁾

The analysis above is valid for semipolar LDs with $\text{In}_x\text{Ga}_{1-x}\text{N}$ QWs where x is less than ~ 0.30 . However, for (11 $\bar{2}$ 2) LEDs it has been observed that the spontaneous emission switches from being polarized along the m -axis for indium compositions less than $\sim 30\%$ to being polarized along the y' -direction for indium compositions greater than $\sim 30\%$.¹⁹⁾ In contrast, for (20 $\bar{2}$ 1) LEDs it has been observed that the spontaneous emission is always polarized along the a -axis and does not vary strongly with indium composition.²⁴⁾ Theoretical calculations for (11 $\bar{2}$ 2) LDs with indium compositions greater than $\sim 30\%$ indicate that the optical gain for LDs with waveguides oriented perpendicular to the y' -direction should be comparable to the optical gain for LDs with waveguides oriented parallel to the y' -direction.^{74,75)} Conversely, theoretical calculations for (20 $\bar{2}$ 1) LDs with indium compositions greater than $\sim 30\%$ indicate that the optical gain for LDs with waveguides oriented perpendicular to the y' -direction should be much less than the optical gain for LDs with waveguides oriented parallel to the y' -direction.⁷⁵⁾ These calculations indicate that (20 $\bar{2}$ 1) LDs with indium compositions greater than $\sim 30\%$ should be oriented parallel to the y' -direction, so mirror facets can be formed only by dry etching or polishing.⁷²⁾ In contrast, these calculations also indicate that (11 $\bar{2}$ 2) LDs with indium compositions greater than $\sim 30\%$ can potentially be oriented perpendicular to the y' -direction, so mirror facets can be formed by cleaving,

which has important implications for the manufacturability of semipolar LDs. However, considering that electrically injected (11 $\bar{2}$ 2) LDs with indium compositions greater than $\sim 30\%$ have yet to be reported, the potential for making semipolar LDs with cleaved facets remains a topic of ongoing investigation.

4.6 Nonpolar III-nitride VCSELs

Unlike edge-emitting LDs, waveguides for VCSELs are always oriented perpendicular to the growth plane,⁷⁶⁾ so only one waveguide orientation needs to be considered. As an example, the polarization of stimulated emission is examined below for m -plane III-nitride VCSELs, although the discussion could be generalized to a -plane III-nitride VCSELs as well. According to the indicatrix construction, the allowed polarizations of modes in a waveguide orientated parallel to the m -axis are parallel to the a -axis and parallel to the c -axis, which are referred to below as the ordinary mode and the extraordinary mode, respectively. The ordinary mode couples to emission from the CH1 band ($\cos^2\alpha = 1$) and the extraordinary mode couples to emission from the CH2 band ($\cos^2\alpha = 1$).^{70,78)} Stimulated emission is expected to be dominated by the ordinary mode because of the much higher hole population in the CH1 band than the CH2 band. Finally, emission from the CH3 band does not couple to either of the waveguide modes because $\cos^2\alpha = 0$ for a waveguide oriented along the m -axis.^{70,78)}

Much like m -plane III-nitride LEDs, emission from m -plane III-nitride VCSELs is typically measured perpendicular to the growth plane. Polarization ratios up to 96% along the a -axis have been measured for m -plane LEDs²⁵⁾ and are limited by the relative hole populations of the CH1 band and the CH2 band. In contrast, the polarization of m -plane VCSELs should be dominated by stimulated emission from the CH1 band, which should reach threshold at much lower carrier densities than the CH2 band and result in polarization ratios that approach 100%.

Previous measurements of m -plane VCSELs (Fig. 17) exhibited polarization along the a -axis with polarization ratios of 72% at levels well above threshold.⁸⁰⁾ However, a Si photodetector was used for collecting the light emission in these measurements, which led to the collection of a significant amount of spontaneous emission and a reduction in the polarization ratio. More recent measurements used a multi-mode optical fiber to eliminate the spontaneous emission from the polarization measurement, resulting in measured polarization ratios of 100% along the a -axis.⁸¹⁾

5. Conclusions and future outlook

In summary, we reviewed recent studies on VB states and polarized optical emission for nonpolar and semipolar III-nitride QWs. Both the physical mechanism and the experimental results were discussed. The reduced crystal symmetry and unbalanced biaxial stress lead to unique valence band structures and optical properties for nonpolar and semipolar III-nitride QW structures, which greatly impact the device performance.

For LEDs, the measurement of polarized light emission from nonpolar and semipolar devices provides a valuable experimental tool to directly study the VB states and optical properties for III-nitride materials. Furthermore, the polarized emission from these devices also has potential appli-

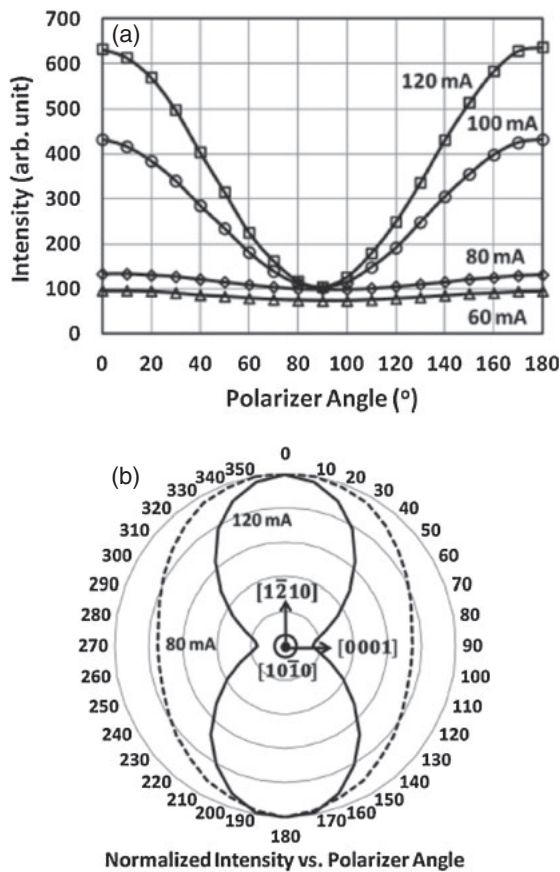


Fig. 17. (a) Dependence of normalized light intensity on polarizer angle for currents both above and below threshold and (b) radial dependence of normalized light intensity on polarizer angle both near and well above threshold for an *m*-plane III-nitride VCSEL.⁸⁰⁾

cations in display systems with low power consumption. However, implementation in these applications will require significant work on topics such as photon recycling.

For LDs, these features have resulted in high performance in nonpolar and semipolar devices compared to conventional *c*-plane devices. As indicated in Fig. 5, the unbalanced biaxial strain in nonpolar and semipolar III-nitride QWs results in a separation in energy between the top two VBs and a change in the curvature of the bands. These changes in the band structure should drastically reduce the density of states that contribute to lasing and are predicted to significantly decrease transparency carrier density and increase differential gain in nonpolar and semipolar III-nitride LDs.^{38,76)}

Acknowledgments

The authors acknowledge the support of the Solid State Lighting and Energy Center at UCSB. Y.-R. Wu was funded by the National Science Council of Taiwan under grant Nos. NSC-102-2221-E-002-194-MY3, MOST-103-2221-E-002-133-MY3, and MOST-103-3113-E-155-001.

1) S. Nakamura, *MRS Bull.* **34** [2], 101 (2009).
 2) R. M. Farrell, E. C. Young, F. Wu, S. P. DenBaars, and J. S. Speck, *Semicond. Sci. Technol.* **27**, 024001 (2012).
 3) P. Waltreit, O. Brandt, A. Trampert, H. T. Grahn, J. Menniger, M. Ramsteiner, M. Reiche, and K. H. Ploog, *Nature* **406**, 865 (2000).

4) F. Bernardini and V. Fiorentini, *Phys. Status Solidi B* **216**, 391 (1999).
 5) A. E. Romanov, T. J. Baker, S. Nakamura, J. S. Speck, and ERATO/JST UCSB Group, *J. Appl. Phys.* **100**, 023522 (2006).
 6) Y. Zhao, S. Tanaka, C. C. Pan, K. Fujito, D. Feezell, J. S. Speck, S. P. DenBaars, and S. Nakamura, *Appl. Phys. Express* **4**, 082104 (2011).
 7) C. C. Pan, S. Tanaka, F. Wu, Y. Zhao, J. S. Speck, S. Nakamura, S. P. DenBaars, and D. Feezell, *Appl. Phys. Express* **5**, 062103 (2012).
 8) R. M. Farrell, D. F. Feezell, M. C. Schmidt, D. A. Haeger, K. M. Kelchner, K. Iso, H. Yamada, M. Saito, K. Fujito, D. A. Cohen, J. S. Speck, S. P. DenBaars, and S. Nakamura, *Jpn. J. Appl. Phys.* **46**, L761 (2007).
 9) K. M. Kelchner, Y. D. Lin, M. T. Hardy, C. Y. Huang, P. S. Hsu, R. M. Farrell, D. A. Haeger, H. C. Kuo, F. Wu, K. Fujito, D. A. Cohen, A. Chakraborty, H. Ohta, J. S. Speck, S. Nakamura, and S. P. DenBaars, *Appl. Phys. Express* **2**, 071003 (2009).
 10) H. H. Huang and Y. R. Wu, *J. Appl. Phys.* **107**, 053112 (2010).
 11) R. Dingle, D. D. Sell, S. E. Stokowski, and M. Ilegems, *Phys. Rev. B* **4**, 1211 (1971).
 12) K. Domen, K. Horino, A. Kuramata, and T. Tanahashi, *Appl. Phys. Lett.* **71**, 1996 (1997).
 13) S. Ghosh, P. Waltreit, O. Brandt, H. T. Grahn, and K. H. Ploog, *Appl. Phys. Lett.* **80**, 413 (2002).
 14) Y. J. Sun, O. Brandt, M. Ramsteiner, H. T. Grahn, and K. H. Ploog, *Appl. Phys. Lett.* **82**, 3850 (2003).
 15) N. F. Gardner, J. C. Kim, J. J. Wierer, Y. C. Shen, and M. R. Krames, *Appl. Phys. Lett.* **86**, 111101 (2005).
 16) R. Sharma, P. M. Pattison, H. Masui, R. M. Farrell, T. J. Baker, B. A. Haskell, F. Wu, S. P. DenBaars, J. S. Speck, and S. Nakamura, *Appl. Phys. Lett.* **87**, 231110 (2005).
 17) H. Masui, A. Chakraborty, B. A. Haskell, U. K. Mishra, J. S. Speck, S. P. DenBaars, and S. Nakamura, *Jpn. J. Appl. Phys.* **44**, L1329 (2005).
 18) M. Funato, M. Ueda, Y. Kawakami, Y. Narukawa, T. Kosugi, M. Takahashi, and T. Mukai, *Jpn. J. Appl. Phys.* **45**, L659 (2006).
 19) M. Ueda, M. Funato, K. Kojima, Y. Kawakami, Y. Narukawa, and T. Mukai, *Phys. Rev. B* **78**, 233303 (2008).
 20) S. Nakagawa, H. Tsujimura, K. Okamoto, M. Kubota, and H. Ohta, *Appl. Phys. Lett.* **91**, 171110 (2007).
 21) M. Kubota, K. Okamoto, T. Tanaka, and H. Ohta, *Appl. Phys. Lett.* **92**, 011920 (2008).
 22) T. J. Badcock, P. Dawson, M. J. Kappers, C. McAleese, J. L. Hollander, C. F. Johnston, D. V. Sridhara Rao, A. M. Sanchez, and C. J. Humphreys, *Appl. Phys. Lett.* **93**, 101901 (2008).
 23) S. You, T. Detchprohm, M. Zhu, W. Hou, E. Preble, D. Hanser, T. Paskova, and C. Wetzel, *Appl. Phys. Express* **3**, 102103 (2010).
 24) T. Kyono, Y. Yoshizumi, Y. Enya, M. Adachi, S. Tokuyama, M. Ueno, K. Katayama, and T. Nakamura, *Appl. Phys. Express* **3**, 011003 (2010).
 25) S. Brinkley, Y. D. Lin, A. Chakraborty, N. Pfaff, D. Cohen, J. S. Speck, S. P. DenBaars, and S. Nakamura, *Appl. Phys. Lett.* **98**, 011110 (2011).
 26) L. Schade, U. T. Schwarz, T. Wernicke, J. Rass, S. Ploch, M. Weyers, and M. Kneissl, *Appl. Phys. Lett.* **99**, 051103 (2011).
 27) Y. Zhao, S. Tanaka, Q. Yan, C. Y. Huang, R. B. Chung, C. C. Pan, K. Fujito, D. Feezell, C. G. Van de Walle, J. S. Speck, S. P. DenBaars, and S. Nakamura, *Appl. Phys. Lett.* **99**, 051109 (2011).
 28) Y. Zhao, Q. Yan, D. Feezell, C. G. Van de Walle, J. S. Speck, S. P. DenBaars, and S. Nakamura, *Opt. Express* **21**, A53 (2013).
 29) M. Suzuki and T. Uenoyama, *Phys. Rev. B* **52**, 8132 (1995).
 30) S. L. Chuang and C. S. Chang, *Phys. Rev. B* **54**, 2491 (1996).
 31) S. H. Wei and A. Zunger, *Appl. Phys. Lett.* **69**, 2719 (1996).
 32) Y. C. Yeo, T. C. Chong, and M. F. Li, *J. Appl. Phys.* **83**, 1429 (1998).
 33) C. Stampfl and C. G. Van de Walle, *Phys. Rev. B* **59**, 5521 (1999).
 34) I. Vurgaftman and J. R. Meyer, *J. Appl. Phys.* **94**, 3675 (2003).
 35) S. H. Park, D. Ahn, and S. L. Chuang, *IEEE J. Quantum Electron.* **43**, 1175 (2007).
 36) S. H. Park, *J. Appl. Phys.* **91**, 9904 (2002).
 37) Q. Yan, P. Rinke, M. Scheffler, and C. G. Van de Walle, *Appl. Phys. Lett.* **95**, 121111 (2009).
 38) W. G. Scheibenzuber, U. T. Schwarz, R. G. Veprek, B. Witzigmann, and A. Hangleiter, *Phys. Rev. B* **80**, 115320 (2009).
 39) M. F. Schubert, J. Xu, J. K. Kim, E. F. Schubert, M. H. Kim, S. Yoon, S. M. Lee, C. Sone, T. Sakong, and Y. Park, *Appl. Phys. Lett.* **93**, 041102 (2008).
 40) C. J. Neufeld, S. C. Cruz, R. M. Farrell, M. Iza, J. R. Lang, S. Keller, S. Nakamura, S. P. DenBaars, J. S. Speck, and U. Mishra, *Appl. Phys. Lett.* **98**, 243507 (2011).
 41) T. Takeuchi, H. Amano, and I. Akasaki, *Jpn. J. Appl. Phys.* **39**, 413 (2000).
 42) A. Bykhovski, B. Gelmont, and M. Shur, *Appl. Phys. Lett.* **63**, 2243 (1993).
 43) S. H. Park and S. L. Chuang, *Phys. Rev. B* **59**, 4725 (1999).
 44) S. H. Park, *Jpn. J. Appl. Phys.* **42**, 5052 (2003).
 45) M. F. Schubert, S. Chhajed, J. K. Kim, E. F. Schubert, and J. Cho, *Appl.*

- Phys. Lett. **91**, 051117 (2007).
- 46) S. Ghosh, P. Waltereit, O. Brandt, H. T. Grahn, and K. H. Ploog, *Phys. Rev. B* **65**, 075202 (2002).
- 47) I. L. Koslow, M. T. Hardy, P. S. Hsu, P.-Y. Dang, F. Wu, A. Romanov, Y.-R. Wu, E. C. Young, S. Nakamura, J. S. Speck, and S. P. DenBaars, *Appl. Phys. Lett.* **101**, 121106 (2012).
- 48) H. Amano, M. Kito, K. Hiramatsu, and I. Akasaki, *Jpn. J. Appl. Phys.* **28**, L2112 (1989).
- 49) A. Chakraborty, B. A. Haskell, S. Keller, J. S. Speck, S. P. DenBaars, S. Nakamura, and U. K. Mishra, *Appl. Phys. Lett.* **85**, 5143 (2004).
- 50) A. Chakraborty, B. A. Haskell, S. Keller, J. S. Speck, S. P. DenBaars, S. Nakamura, and U. K. Mishra, *Jpn. J. Appl. Phys.* **44**, L173 (2005).
- 51) Y. Zhao, J. Sonoda, I. Koslow, C. C. Pan, H. Ohta, J.-S. Ha, S. P. DenBaars, and S. Nakamura, *Jpn. J. Appl. Phys.* **49**, 070206 (2010).
- 52) Y. Zhao, J. Sonoda, C. C. Pan, S. Brinkley, I. Koslow, K. Fujito, H. Ohta, S. P. DenBaars, and S. Nakamura, *Appl. Phys. Express* **3**, 102101 (2010).
- 53) M. D. Craven, S. H. Lim, F. Wu, J. S. Speck, and S. P. DenBaars, *Appl. Phys. Lett.* **81**, 469 (2002).
- 54) T. J. Baker, B. A. Haskell, F. Wu, J. S. Speck, and S. Nakamura, *Jpn. J. Appl. Phys.* **45**, L154 (2006).
- 55) K. Fujito, K. Kiyomi, T. Mochizuki, H. Oota, H. Namita, S. Nagao, and I. Fujimura, *Phys. Status Solidi A* **205**, 1056 (2008).
- 56) H. Masui, H. Yamada, K. Iso, H. Hirasawa, N. N. Fellows, J. S. Speck, S. Nakamura, and S. P. DenBaars, *Phys. Status Solidi A* **205**, 1203 (2008).
- 57) H. Masui, H. Yamada, K. Iso, S. Nakamura, and S. P. DenBaars, *Appl. Phys. Lett.* **92**, 091105 (2008).
- 58) A. A. Yamaguchi, *Jpn. J. Appl. Phys.* **46**, L789 (2007).
- 59) Y. Enya, Y. Yoshizumi, T. Kyono, K. Akita, M. Ueno, M. Adachi, T. Sumitomo, S. Tokuyama, T. Ikegami, K. Katayama, and T. Nakamura, *Appl. Phys. Express* **2**, 082101 (2009).
- 60) S. Yamamoto, Y. Zhao, C. C. Pan, R. B. Chung, K. Fujito, J. Sonoda, S. P. DenBaars, and S. Nakamura, *Appl. Phys. Express* **3**, 122102 (2010).
- 61) Y. Zhao, Q. Yan, C. Y. Huang, S. C. Huang, P. S. Hsu, S. Tanaka, C. C. Pan, Y. Kawaguchi, K. Fujito, C. G. Van de Walle, J. S. Speck, S. P. DenBaars, S. Nakamura, and D. Feezell, *Appl. Phys. Lett.* **100**, 201108 (2012).
- 62) Y. Zhao, S. H. Oh, F. Wu, Y. Kawaguchi, S. Tanaka, K. Fujito, J. S. Speck, S. P. DenBaars, and S. Nakamura, *Appl. Phys. Express* **6**, 062102 (2013).
- 63) Q. Yan, P. Rinke, M. Scheffler, and C. G. Van de Walle, *Appl. Phys. Lett.* **97**, 181102 (2010).
- 64) R. B. Chung, Y. D. Lin, I. Koslow, N. Pfaff, H. Ohta, J. Ha, S. P. DenBaars, and S. Nakamura, *Jpn. J. Appl. Phys.* **49**, 070203 (2010).
- 65) H. Masui, H. Yamada, K. Iso, J. S. Speck, S. Nakamura, and S. P. DenBaars, *J. Soc. Inf. Disp.* **16**, 571 (2008).
- 66) J. F. Nye, *Physical Properties of Crystals: Their Representation by Tensors and Matrices* (Oxford University Press, Oxford, U.K., 1985) 2nd ed.
- 67) S. Shokhovets, R. Goldhahn, G. Gobsch, S. Piekh, R. Lantier, A. Rizzi, V. Lebedev, and W. Richter, *J. Appl. Phys.* **94**, 307 (2003).
- 68) W. G. Scheibenzuber, U. T. Schwarz, R. G. Veprek, B. Witzigmann, and A. Hangleiter, *Phys. Status Solidi C* **7**, 1925 (2010).
- 69) J. Rass, T. Wernicke, W. G. Scheibenzuber, U. T. Schwarz, J. Kupec, B. Witzigmann, P. Vogt, S. Einfeldt, M. Weyers, and M. Kneissl, *Phys. Status Solidi: Rapid Res. Lett.* **4**, 1 (2010).
- 70) J. Rass, T. Wernicke, S. Ploch, M. Brendel, A. Kruse, A. Hangleiter, W. Scheibenzuber, U. T. Schwarz, M. Weyers, and M. Kneissl, *Appl. Phys. Lett.* **99**, 171105 (2011).
- 71) J. Rass, T. Wernicke, R. Kremzow, W. John, S. Einfeldt, P. Vogt, M. Weyers, and M. Kneissl, *Phys. Status Solidi A* **207**, 1361 (2010).
- 72) P. S. Hsu, R. M. Farrell, J. J. Weaver, K. Fujito, S. P. DenBaars, J. S. Speck, and S. Nakamura, *IEEE Photonics Technol. Lett.* **25**, 2105 (2013).
- 73) D. S. Sizov, R. Bhat, J. Napierala, C. Gallinat, K. C. Song, and C. E. Zah, *Appl. Phys. Express* **2**, 071001 (2009).
- 74) K. Kojima, A. A. Yamaguchi, M. Funato, Y. Kawakami, and S. Noda, *Jpn. J. Appl. Phys.* **49**, 081001 (2010).
- 75) W. G. Scheibenzuber and U. T. Schwarz, *Phys. Status Solidi B* **248**, 647 (2011).
- 76) L. A. Coldren, S. W. Corzine, and M. L. Masanovic, *Diode Lasers and Photonic Integrated Circuits* (Wiley, New York, 2012) 2nd ed.
- 77) D. Feezell and S. Nakamura, in *Semiconductor Lasers: Fundamentals and Applications*, ed. A. Baranov and E. Tournie (Woodhead Publishing, Cambridge, U.K., 2013) 1st ed.
- 78) L. Schade, U. T. Schwarz, T. Wernicke, M. Weyers, and M. Kneissl, *Phys. Status Solidi B* **248**, 638 (2011).
- 79) K. Okamoto, H. Ohta, S. F. Chichibu, J. Ichihara, and H. Takasu, *Jpn. J. Appl. Phys.* **46**, L187 (2007).
- 80) C. Holder, J. S. Speck, S. P. DenBaars, S. Nakamura, and D. Feezell, *Appl. Phys. Express* **5**, 092104 (2012).
- 81) C. O. Holder, J. T. Leonard, R. M. Farrell, D. A. Cohen, B. Yonkee, J. S. Speck, S. P. DenBaars, S. Nakamura, and D. F. Feezell, submitted to *Appl. Phys. Lett.*



Yuji Zhao is an Assistant Project Scientist in the Materials Department at the University of California, Santa Barbara (UCSB). He received the Ph.D. degree in Electrical and Computer Engineering from UCSB in 2012, and the B.S. degree in Microelectronics from Fudan University, China in 2008.



Robert M. Farrell is a Postdoctoral Researcher in the Materials Department at the University of California, Santa Barbara (UCSB). He received the Ph.D. degree in Electrical and Computer Engineering (ECE) from UCSB in 2010, and the B.S. degree in ECE from University of Illinois at Urbana-Champaign in 2003.



Yuh-Renn Wu received the B.S. in Physics and the M.S. degree in Electrical Engineering from National Taiwan University, Taipei, Taiwan, in 1998 and 2000, respectively, and the Ph.D. degree in Electrical Engineering from the Department of Electrical Engineering and Computer Science, University of Michigan, Ann Arbor, MI, USA, in 2006. He is currently an Associate Professor with the Institute of Photonics and Optoelectronic, National Taiwan University.



James S. Speck is a Professor in the Materials Department at the University of California Santa Barbara (UCSB). At UCSB, he has worked extensively on the materials science of GaN and related alloys include elucidating basic growth modes and defect generation, developing MBE growth of GaN, and developing nonpolar and semipolar GaN. He received the Quantum Device Award from the International Symposium on Compound Semiconductors in 2007, the JJAP Best Paper Award in 2008, the IEEE Photonics Society Aron Kressel Award in 2010, and was named an inaugural MRS Fellow in 2008 and an APS Fellow in 2009.